Quantitative 3D histochemistry reveals region-specific amyloid-β reduction by the antidiabetic drug netoglitazone

Francesca Catto[1,2§], Ehsan Dadgar-Kiani[3,4§], Daniel Kirschenbaum[1§], Athena Economides[1], Anna Maria Reuss[1], Chiara Trevisan[1], Davide Caredio[1], Delic Mirzet[1], Lukas Frick[1], Ulrike Weber-Stadlbauer[3,4], Sergey Litvinov[9,10], Petros Koumoutsakos[10], Jin Hyung Lee[5,6,7,8*+], Adriano Aguzzi[1*+]

[1]Institute of Neuropathology, University Hospital Zurich, University of Zurich, Schmelzbergstrasse 12, CH-8091 Zurich, Switzerland

[2]IMAI MedTech, Wagistrasse 18, 8952 Schlieren, Zurich, Switzerland

[3]Institute of Veterinary Pharmacology and Toxicology, University of Zurich, Winterthurerstrasse 260, 8057 Zürich

[4]Neuroscience Center Zurich, University of Zurich and ETH Zurich, 8057 Zurich, Switzerland.

[5]Department of Neurology and Neurological Sciences, Stanford University, CA 94305, USA

[6]Department of Bioengineering, Stanford University, Stanford, CA 94305, USA

[7]Department of Electrical Engineering, Stanford University, CA 94305, USA

8Department of Neurosurgery, Stanford University, Stanford, CA 94305, USA

[9]Computational Science and Engineering Laboratory, ETH Zürich, Clausiusstrasse 33, 8092, Zurich, Switzerland

[10]Computational Science and Engineering Laboratory, Harvard University, Cambridge, MA 02138, United States.

[§]Co-first authors; equal contribution

[+]Co-corresponding authors; equal contribution

[*]Correspondence: adriano.aguzzi@usz.ch, ljinhy@stanford.edu

Abstract

A hallmark of Alzheimer's disease (AD) is the extracellular aggregation of toxic amyloid-beta (Aβ) peptides in form of plaques. Here, we identify netoglitazone, an antidiabetic compound previously tested in humans, as an Aβ aggregation antagonist. Netoglitazone improved cognition and reduced microglia activity in a mouse model of AD. Using quantitative whole-brain three-dimensional histology (Q3D), we precisely identified brain regions where netoglitazone reduced the number and size of Aβ plaques. We demonstrate the utility of Q3D in preclinical drug evaluation for AD by providing a high-resolution brain-wide view of drug efficacy. Applying Q3D has the potential to improve pre-clinical drug evaluation by providing information that can help identify mechanisms leading to brain region-specific drug efficacy.

Significance statement

Alzheimer’s disease (AD) is the most prevalent neurodegenerative disease. Its primary symptom is progressive cognitive decline, which impairs executive brain functions and deprives patients of their autonomy in life. Experimental and clinical evidence points to the critical pathophysiological role of the amyloid-beta (Aβ) peptide. Despite some limited successes in AD immunotherapy targeting Aβ, AD is still incurable. Here, we use an innovative pipeline for accurate whole-brain measurements of Aβ load to test the efficacy of the antidiabetic compound, netoglitazone. We found that netoglitazone decreases Aβ burden in certain brain areas but not in others. Region-specific assessment of anti-Aβ efficacy may be useful in the development of effective drugs against Alzheimer’s disease.

Keywords: Alzheimer's disease; amyloid beta aggregates; amyloid plaques; peroxisome proliferators activated receptor-gamma; netoglitazone; microglia; neuroinflammation.

Introduction

Alzheimer's disease (AD) is a prevalent neurodegenerative disease which causes an inexorable decline in cognitive abilities, affecting the life of patients and of their caregivers and eventually leading to dementia and death [1]. Given that the strongest risk factor for AD is age, and considering that life expectancy is increasing in most parts of the world, it is anticipated that the incidence of AD will increase.

In AD, the amyloidogenic peptide amyloid beta (Aβ) is liberated from its precursor protein APP and aggregates into fibrils, giving rise to structures termed “neuritic plaques” by Alois Alzheimer. These aggregated species serve as templates and seeds for the nucleation of further Aβ [2-4] aggregation. According to the amyloid cascade hypothesis [5], Aβ aggregation is the primary cause of AD which induces all downstream aspects of neurodegeneration (aggregation of Tau protein, astrocyte and microglia activation, and eventually neuronal loss).

While familial forms of AD are often caused by Aβ overexpression, there is a continuing debate about the importance of Aβ in sporadic AD [6]. Many studies have shown that total Aβ deposition in humans correlate poorly with cognitive decline [7], and intellectually healthy individuals can carry remarkable Aβ loads in their brains. Moreover, therapeutic trials with the anti-Aβ antibodies, crenezumab, aducanumab, solanezumab, lecanemab, and gantenerumab have delivered marginal results despite well-documented efficacious pharmacodynamics and impressive removal of brain Aβ. [8-10]. In addition, severe side effects have been reported, including brain edema and bleeding [11, 12]. Coupled with the long-term treatment duration and the significant costs associated with therapy, it is crucial to gain a deeper understanding of the disease mechanisms and explore more effective treatment strategies.

While none of the clinical trials with anti-Aβ antibodies have yet delivered substantial therapeutic results, it is interesting to note that some antibodies had no discernible effect on the course of the disease whereas others appear to yield statistically meaningful, though very limited, beneficial effects[13-16]. The failure rate of AD clinical trials may be attributed to multiple reasons. Each of these antibodies target different epitopes and even different aggregational states and conformers of Aβ, and such parameters are likely to influence their therapeutic efficacy. However, the expression of APP and of the components responsible for its catabolic conversion into Aβ (e.g. BACE-1, presenilins, nicastrin, and several other proteins) is known to vary by anatomical brain region [16-20]. This would result in distinct region-specific drug efficacies. In addition, many of the brain functions affected by AD are related to specific brain regions, not necessarily overlapping with the regiospecificity of AD-drugs [21, 22]. However, the available data on the regional distribution of Aβ in the brain are limited, mostly due to lack of suitable technology. Amyloid load can be measured in clinical

and preclinical studies using various techniques, including PET imaging, stereometric immunohistochemistry, ELISA, and western blotting [23-27]. However, these approaches either lack scalability to sample the entire brain (histology) or have no or very low spatial resolution (ELISA, PET). Taking into account the highly compartmentalized structure of the brain and region specific functions and symptoms, selective vulnerability, and pharmacodynamics [28], the testing of AD drugs requires imaging tools that are highly sensitive and can afford high spatial resolution.

Investigation of cheaper and less invasive therapies, such as lifestyle interventions, non-drug interventions, and repurposed drugs, may provide alternative approaches that can complement or replace current treatments for AD [29]. In addition, repurposing existing drugs already approved for other diseases may provide a more efficient and cost-effective approach to developing new treatments for AD [30]. The present work builds on a previous study that screened compounds to target Aβ aggregation in vitro and identified netoglitazone, an FDA-approved thiazolidinedione (TZD) family antidiabetic compound, as an Aβ modifier from *in vitro* [31]. Here, we present a standardized procedure for screening anti-amyloid compounds in vivo. Our pipeline includes high-resolution 3D pharmacodynamic analysis, RNA sequencing, and behavioral assays to test molecules at the brain level. The in vivo tests show that netoglitazone reduces Aβ load and microglia activity in a region-specific manner, and improves cognition in Alzheimer's mouse models. Our approach is generalizable and applicable to any anti-Aβ compound.

Results

Long-term treatment with netoglitazone significantly reduces cognitive deficits in APP/PS1 mice

Previous findings showed that netoglitazone decreases the aggregation of Aβ fibrils in cell-free in vitro and in vivo models of C. elegans, as well as penetrates the blood-brain barrier of mice when administered orally [31]. Thus, we investigated the removal of neuritic plaques by netoglitazone in APPPS1 mice [32]. We administered netoglitazone orally at a low (25mg/ml) or high (75mg/ml) dose, beginning at the age of two months and continuing for 90 or 180 days, referred to as "short-term treatment" and "long-term treatment", respectively (Figure 1A). During the long-term treatment, blood samples were taken at 7 and 28 days after initiating the treatment, and drug levels were quantified (Figure 1A). The measured drug concentrations in plasma were 6297 ng/ml and 6272 ng/ml (SD = 6736) at 7 and 28 days, respectively, after starting the low dose treatment. For the high dose treatment, the measured drug concentrations in plasma were 21834 ng/ml and 13544 ng/ml (SD = 2364) at 7 and 28 days, respectively, after starting the treatment. These findings indicate that the drug attains stable plasma levels over the course of a month (Figure 1B). We then investigated whether high doses of netoglitazone could improve behavioral outcomes in APPPS1 mice [32]. The behavioral response of mice was examined using a range of paradigms and the outcomes were contrasted with those observed in untreated APPPS1 mice. To control for non-specific effects, wild-type (WT) littermate mice were also tested after receiving either a high dose of netoglitazone or phosphate-buffered saline (PBS) orally. All behavioral tests were conducted when the mice were approximately 8 months old, shortly before receiving their final daily oral administration of the drug. The results showed that netoglitazone treatment led to significant improvements in contextual fear memory, innate anxiety-like behaviors, and temporal order memory, compared to non-treated mice (Figure 1C,D,E). However, no improvements were observed in basal locomotor activity or spatial recognition memory (Supplementary Figure 1).

The anxiety-like behaviors of APPPS1 and WT mice were evaluated by conducting the light/dark box paradigm. Treated APPPS1 mice showed an increased distance moved in the light compartment as compared to untreated animals. These results indicate that netoglitazone has anxiolytic effects in APPPS1 animals while not affecting their general maze exploration (Figure 1C).

To assess the effect of netoglitazone on contextual fear memory, the freezing behavior during training and testing was analyzed as previously described [33]. The percentage of time spent displaying freezing behavior was calculated for each condition and time-point (24h and 48h after conditioning). Results showed that after 24 hours, netoglitazone-treated mice displayed

158 significantly more freezing behavior compared to the PBS-treated mice, regardless of
159 genotype. 48 hours after conditioning, both APPPS1 and WT mice treated with netoglitazone
160 exhibited increased freezing time compared to their respective PBS-treated controls,
161 indicating a potential deficit in fear memory in untreated animals (Figure 1D).

162 To assess the potential effect of netoglitazone on temporal memory, the temporal order
163 memory test was conducted on both APPPS1 and WT mice. The results showed that APPPS1
164 mice exhibited impaired temporal order memory, whereas no such impairment was observed
165 in WT mice. However, the impairment in temporal order memory observed in the
166 netoglitazone-treated APPPS1 group was restored to control levels (Figure 1E).

167 These findings provide evidence for the efficacy of netoglitazone in improving the temporal
168 short-term memory of APPPS1 mice.

169 Furthermore, we assessed the spatial memory abilities of the animals using the Y-maze
170 paradigm. We observed no significant differences in the time spent in the novel arm among
171 the different treatments and genotypes, indicating that netoglitazone treatment did not improve
172 short-term spatial memory (Supplementary Figure. 1A, 1B). We further evaluated the effect
173 of netoglitazone on basal locomotor activity by subjecting APPPS1 and WT mice to the open
174 field paradigm. Our findings indicate that netoglitazone treatment led to a trend towards a
175 decrease in basal locomotor activity in WT mice, as evidenced by a reduction in the distance
176 travelled compared to PBS-treated WT mice. However, there was no effect on basal locomotor
177 activity in APPPS1 mice, as both treated and control mice showed a similar total distance
178 moved (Supplementary Figure 1C).

179

180 *Voxel-based statistics of whole-brain drug efficacy shows regional and dose-dependent*
181 *effectiveness of netoglitazone in decreasing Aβ aggregates*

182 To assess the effects of netoglitazone on the amyloid burden in the brain, two groups of 2-
183 month old APPPS1 mice (30 mice/group) were treated daily for a short-term (90 days) or long-
184 term (180 days) period with 100-300 µL of either a low dose (25 mg/ml day/mouse) or a high
185 dose of netoglitazone (75 mg/ml day/mouse) by oral administration, after which they were
186 sacrificed. PBS was administered to control mice. All brains were extracted and subjected to
187 focused electrophoretic tissue clearing (FEC) [34], Aβ staining, and whole-brain imaging
188 (Supplementary Figure 2A). The brains were rendered transparent and luminescent
189 conjugated polythiophenes (LCPs) [35] were used to label the amyloid plaques. These
190 plaques were then imaged across the whole brain with a light sheet fluorescence microscope
191 [36]. Plaques were automatically segmented and regionally quantified using previously
192 described methods [34]. The average plaque count and plaque size within 25-µm voxels were

193 determined for each treatment cohort and presented in a heatmap to show the difference in
194 number and size of plaques between multiple brain areas and treatment conditions
195 (Supplementary Figure 3A-B). To intuitively visualize the therapeutic effect of the two dosages
196 of netoglitazone in the two cohorts, we compared 25-μm voxels corresponding to the average
197 number or plaque size between cohorts (short-term or long-term treatment) and dosages by
198 inferential statistics [34] and depicted them for the whole brain. Voxels revealing a decrease
199 or increase in plaque count and size were highlighted with two different scale bars. This
200 allowed us to identify voxels significantly altered by the action of netoglitazone and to generate
201 digitally resliced p-value heatmaps ($p < 0.05$) in coronal sections. (Figure 2, Figure 3 and
202 Supplementary Videos). We also investigated the differences in plaque count and mean size
203 between treatment groups in 52 neuroanatomical regions defined by the Allen Brain Atlas [37]
204 (Figure 2, Figure 3 and Supplementary File 1). In the low-dose cohorts, heatmaps of p-values
205 at voxel level showed that the effect of short-term treatment with netoglitazone promoted a
206 decrease in the count of plaques in certain areas belonging primarily to the olfactory, striatal,
207 and thalamic areas compared to PBS-treated mice (Figure 2**Figure 2**A), while long-term
208 treatment reduced the count of plaques in areas belonging primarily to the olfactory, hindbrain,
209 and visual areas (Figure 2B). However, the low dose long-term treatment also induced a
210 scattered increase in the hippocampal, cortical, striatal, and midbrain areas.

211 With regard to the high-dose short-term treatment cohort, the drug's effect in reducing the
212 count of plaques was observed extensively in the hindbrain, midbrain, striatum, and olfactory
213 areas (Figure 2C). In a similar pattern, a decrease in the count of plaques following long-term
214 high-dose treatment was observed in certain areas of the olfactory, striatum, pallidum,
215 hindbrain, and midbrain regions (Figure 2D). In addition, we studied the effect of the drug on
216 mean plaque size. Using voxel-p-value maps, we observed that a short-term treatment with
217 low-dose netoglitazone resulted in a strong and widespread decrease in plaque size in
218 olfactory, hippocampal, striatal, thalamic, and midbrain areas (Figure 3A). When the low dose
219 of drug was administered for long-term, an increase in plaque size was mainly detected in
220 optical cortex, visual area, hippocampus, striatum, and hindbrain. (Figure 3B). When we
221 administered a high dose of netoglitazone for short-term, we observed a significant decrease
222 in plaque size in hippocampus, striatum, thalamus, hypothalamus, midbrain, and hindbrain,
223 but we also observed a diffuse increase in olfactory, hippocampal, cortical, and striatal areas
224 (Figure 3C). Examining long-term high-dose treatment, we observed a significant decrease in
225 plaque size in orbital cortex, olfactory area, hippocampus, thalamus, hypothalamus, midbrain,
226 and hindbrain regions (Figure 3D). In all the cases described above, we have noticed a parallel
227 distribution of effects in the two hemispheres.

In summary, when given at a high dose over extended periods, netoglitazone was highly effective in reducing both the number and average size of plaques. Conversely, the low dose of netoglitazone showed greater efficacy in reducing plaque count and size when administered for shorter durations. Nevertheless, there were instances where plaque average size increased unfavorably (Supplementary Figure 3C).

We further validated our 3D histology results with 2D immunohistochemistry (IHC) and immunofluorescence microscopy (IF). A group of 2-month old APPPS1 mice (30 mice) were treated daily for 180 days with either a low-dose (25mg/ml day/mouse) or a high-dose of netoglitazone (75mg/ml day/mouse) by oral administration. Control treatments included oral administration of PBS. Mice were sacrificed 180 days after the start of the treatment. Brains were split in two hemispheres. 18 slides of 6 µm each (6 slides per treatment dosage/control) were cut from each hemisphere and subjected to Aβ staining with an anti-Aβ antibody. 3 slides/condition were stained for both IHC and IF and imaged with either a Zeiss Axiophot light microscope or a Leica SP5 confocal microscope (Supplementary Figure 4A). Whole sagittal slices (for IHC) or smaller selected areas of cortex, hippocampus and thalamus (for IF) were analyzed, and the number of pixels covered by plaques were counted with ILASTIK [38] (Supplementary Figure 4B) to evaluate the efficacy of the drug in reducing plaque count using quantitative 2D analysis did not yield any significant differences between the treated and control groups of mice. Consequently, we were unable to demonstrate any substantial effect of the drug in reducing the number of plaques in the brain tissue using 2D histology. While this method is a useful tool for evaluating changes in plaque morphology and distribution, it may not be sensitive enough to detect subtle differences in plaque count between the groups.

Netoglitazone decreases microglia activation in a dose-dependent manner

To test the effect of netoglitazone on neuroinflammation and gliosis, 3 mice per group (3 high-dose, 3 low-dose, 3 PBS-treated mice) were treated daily for 180 days with either a low-dose (25mg/ml day/mouse) or a high-dose of netoglitazone (75mg/ml day/mouse) by oral administration. Control treatments included oral administration of PBS. Mice were sacrificed 180 days after the start of the treatment, their brains were extracted, and the hemispheres were separated by a sagittal cut. The right hemispheres were subjected to a modified version of DISCO clearing [39] and stained for microglia with Iba1 antibody. For imaging, a 640nm laser and a F76 647SG long pass filter were used. Transparent whole hemispheres were imaged at 3.26 × 3.26 × 3 μm^3 (X × Y × Z) voxel size resolution. Raw microscopy images (Supplementary Figure 3) were transformed and registered to the coordinate space of the Allen Brain Atlas [40] with cubic-voxel side-resolution of 25 µm. We performed automated

263 microglia segmentation and regional density quantification using a customized computational
264 pipeline aimed at high-speed processing of half-brain mouse datasets. The pipeline consists
265 of three main steps: (i) image restoration aimed at reducing intensity undulations of the
266 background and increasing signal to noise ratio [95], (ii) microglia segmentation in 3D using
267 intensity-based pixel classification, and (iii) regional microglia-density quantification.
268 Techniques such as parallel programming for shared memory architectures (OpenMP) and
269 memory mapping are employed to reduce the processing time. More details for the pipeline
270 can be found in the Methods section and the corresponding github repository. After
271 segmentation, we generated 3D maps of statistically affected voxels by computing a voxel-
272 wise p-value, between each of the treated cohorts and the PBS-treated cohort. We measured
273 the total volume covered by microglia in each hemisphere of the three different cohorts, and
274 observed a significant reduction in Iba1^{+} microglia in mice treated with the high dose of the
275 drug (1.98 mm^3) compared to those treated with PBS (4.15 mm^3). Surprisingly, mice treated
276 with the low dose of the drug showed an increase in Iba1^{+} microglia in the brain stem,
277 hypothalamus and thalamus regions compared to PBS (Figure 4A). Next, we analyzed the
278 correlation between the decrease and increase in plaque density and microglia volume in mice
279 that received long-term treatment. On this end, we performed a spatial colocalization of the
280 statistically significant voxel maps for microglia and plaques, and computed the number of
281 voxels that displayed a statistically significant effect (increase or decrease) in both microglia
282 and plaque maps. There was a high correlation between the decrease of plaques and
283 decrease of microglia in mice treated with a high drug dose, while in mice treated with a low
284 dose the decrease in microglia was highly correlated with the increase in plaques (Figure 4B).

285

286 *Netoglitazone alters gene expression in a dose-dependent manner*

287 To investigate the gene expression changes promoted by the different netoglitazone
288 treatments, we verified the genetic changes following the two different dosages of
289 netoglitazone after long-term treatment. 17 mice (7 high-dose, 3 low-dose, 7 PBS-treated
290 mice) were treated for 180 days. The hemispheres of these mice were separated, and one
291 hemisphere per sample was analyzed for the differentially expressed genes (DEGs) by RNA
292 sequencing (RNA-Seq). Treatment with low-dose netoglitazone promoted a significant change
293 in expression of 361 DEGs compared to the PBS-treated mice. 135 genes were upregulated,
294 whereas 226 genes were downregulated (Supplementary Files 2-5). Among the top 20 most
295 significantly upregulated DEGs, we found several members of the immediate early gene (IEG)
296 family, including Fos, Arc, Erg4, Fosb, Fosl2, Apold1, Junb, Dusp1, Ier2, Egr3, Nptx2 and Btg2
297 (Figure 5 and Supplementary Files 3,5). By contrast, the most significantly downregulated
298 genes seemed to be involved in several independent processes, with the most relevant in

regulation of circadian rhythm (DBP), collagen production (Col6a1), modulation of neuronal toxicity (Wsb1), and drug metabolism (Fmo2). The number of DEGs whose expression was significantly altered following high-dose netoglitazone administration, compared with control, was very low. The significantly increased genes turned out to be only five (CD68, Gpnmb, Serpina3n, Cd180, Ccl3), mainly related to inflammatory mechanisms and immune response, while the decreased gene was only one (Gm26917). (Figure 5 and Supplementary Files 2,4).

Discussion

There is increasing evidence that complete, rapid amyloid clearance could be key to attenuating the progression of AD [41]. Therefore, identifying drugs that effectively disrupt Aβ aggregation could be a valuable strategy to combat AD. PPARγ receptor activation can counteract the pro-inflammatory and pro-oxidant environment in the CNS, central to AD pathogenesis, making them an attractive pharmacological target [42-48]. Pre-clinical and clinical studies have shown that TZDs, a group of PPARγ agonists, can reduce Aβ generation and release, improve learning and memory, and decrease amyloid pathology in a time- and dose-dependent manner [49-53]. However, the therapeutic efficacy of these molecules in clinical trials was found to be modest, possibly due to imprecise assessments of their impact on Aβ plaque load [54-58]. More comprehensive methods may be required to evaluate the effectiveness of these drugs.

Here, we aimed to evaluate the efficacy of the experimental anti-diabetic drug netoglitazone, a PPARγ agonist belonging to the TZD group, in treating, preventing or inhibiting the formation, deposition, accumulation or persistence of amyloid aggregates in vivo [59]. To overcome the limitations of previous studies, we used three-dimensional histology and computational methods to holistically evaluate the efficacy of netoglitazone and to uncover differences at the regional anatomical level. Netoglitazone has shown promise in previous drug-repurposing strategies and in vitro assays by decreasing fibril mass concentration in a dose-dependent manner and improving the fitness of AD worm models (C. elegans) by reducing the number of aggregates that are formed [31]. These results suggest that netoglitazone may have anti-amyloid properties and be effective in treating AD, which motivated us to further investigate its efficacy in vivo.

We studied the effects of netoglitazone in an animal model of AD and found that a high dose can improve fear and temporal memory in APPPS1 mice. Using Q3D analysis [60], we discovered that the impact of the drug on plaques depended on the dosage and administration period, leading to both decreased and increased plaques in various brain regions. Our study found that higher doses of the drug had a greater and more optimal impact in reducing plaque number at long-term treatment, while lower doses were better at reducing both plaque number and size in short-term treatment. Additionally, we found that the boundaries of drug action did not always correspond to historically defined neuroanatomical areas, suggesting the existence of hitherto unrecognized local modifiers within the brain of hosts. Through Q3D, we were able to identify both favorable and unfavorable changes in amyloid quantity that could not have been detected with traditional biochemistry or histology techniques.

Our research suggests that the varying effects of netoglitazone, contingent on the dose and duration of administration, may be linked to the distinctive expression levels of PPARγ receptors in the brain, different cell types, and the specific stage of the disease [61]. To gain insights into this phenomenon, we examined pioglitazone, a drug similar to netoglitazone, which has been found to exert control over PPARγ receptor target genes in neural cells in a dose-dependent and cell-specific manner. The study of pioglitazone sheds light on the underlying mechanisms that determine the beneficial or adverse effects of netoglitazone, varying according to the dosage used and the specific cell types involved [61].

An additional factor that may contribute to the varying effects of netoglitazone is the disparity in PPARγ receptor expression between males and females [61] Our study did not differentiate between male and female groups. Furthermore, the present study is limited by the spatial resolution of our Q3D mesoSPIM equipment which does not allow for discriminating structures smaller than 3 µm isotropic. For this reason, Q3D could be optimally combined with orthogonal techniques such as single-cell sequencing and spatial transcriptomics, thereby providing a comprehensive and precise descriptions of spatial drug responses .

Our 3D histology study revealed that the efficacy of netoglitazone in reducing amyloidosis exhibits spatial-temporal specificity. This intriguing finding suggests that the drug's effectiveness in combating amyloid plaques might vary based on the location within the brain and the stage of disease progression. The implications of these observations extend beyond netoglitazone and may have generalizable implications for anti-amyloid therapies.

In summary, our study highlights the intricate relationship between netoglitazone's effects and dosage, administration duration, cell type, disease stage, and potentially even gender differences in PPARγ receptor expression. Understanding these multifaceted factors can contribute to optimizing therapeutic approaches and uncovering novel treatment strategies for amyloid-related disorders and possibly other neurodegenerative diseases.

Inflammation and gliosis are histological hallmarks of AD and can be observed in APPPS1 mice from an early age on [62]. Aβ plaque-associated reactive microgliosis is seen in rodent models of AD and human cases, indicating that Aβ deposition leads to microglial activation [63-66]. PPARγ agonists have been shown to inhibit microglial activation and inflammation, making them a potential therapeutic option for AD [67-69]. Q3D allows for precisely quantifying the changes in microglia volume following long-term treatment with netoglitazone. We found that high-dose netoglitazone significantly reduced the total volume of microglia throughout the brain, particularly in the cortex, and this correlated with a decrease in Aβ plaques. In contrast, low-dose netoglitazone had a mixed effect on microglia in a spatially-dependent manner.

These findings suggest that a long-term high dose of netoglitazone may reduce inflammation and enhance the phagocytic activity of microglia, which facilitates the removal of Aβ deposits.

We measured gene expression changes in APPPS1 mice treated with different doses of netoglitazone and compared them to PBS. Among the genes that showed a significant difference between low-dose netoglitazone and PBS, the 20 most upregulated genes were immediate early genes (IEGs) associated with neuronal plasticity and memory formation [70]. This suggests that low-dose treatment stimulated a stress and inflammation response, potentially due to the drug's localized efficacy throughout the brain [71-75]. On the other hand, high-dose treatment led to a small number of differentially expressed genes, mostly related to microglia activation and immune defense mechanisms, indicating a decrease in amyloidosis and inflammation throughout the brain [76-81]. These findings are consistent with our observations from the whole-brain maps.

Beyond its significance in the evaluation of netoglitazone in AD, the present study showcases Q3D as an advanced technique capable of identifying phenomena that had gone undetected by conventional microscopy.

Author Contributions

The contributions to this research were as follows: FC planned the experimental design, conducted the experiments, and wrote the manuscript. DK contributed significantly to the experimental design and assisted in the preparation of the manuscript. FC and DC were responsible for data analysis. EDK performed 3D plaque image analysis. AE, SL and PK jointly conducted the analysis of 3D images of microglia. Figure preparation was a collaborative effort involving FC, EDK and AE. AMR and CT provided key support in the execution of the experiments, while DM and UW were integral to the animal experiments. LF brought key expertise in the task of stitching 3D images. The project was overseen by JHL, PK and AA, who not only supervised the entire work and contributed to the manuscript, but also played a key role in securing financial support.

Materials and Methods

APPS1 mice

APPPS1 transgenic mice were used in the study, which co-express the Swedish mutation K670M/N671L and PS1 mutation L166P under the control of the neuron-specific Thy-1 promoter on a C57BL/6 genetic background [32]. APPPS1 mice were habituated ahead of the study to voluntarily drink condensed milk formulation from a pipette. The condensed milk used in the study is commercially available (Migros) and contains milk, sugar, stabilizer E339. Body weight was measured ahead of commencing the study to calculate the dose of netoglitazone for each mouse and to calculate the total blood volume.

Animal treatments and tissue preparation

All animal experiments were carried out in strict accordance with the Rules and Regulations for the Protection of Animal Rights (Tierschutzgesetz and Tierschutzverordnung) of the Swiss Bundesamt für Lebensmittelsicherheit und Veterinärwesen and were pre-emptively approved by the Animal Welfare Committee of the Canton of Zürich (permit 040/2015). APPPS1 male and female mice were treated daily orally with netoglitazone (Wren Therapeutics, Cambridge UK) diluted in condensed milk (Migros, Switzerland) and PBS. The administered dosages were either with 75mg/ml (high-dose) or 25mg/ml (low-dose). The treatment duration was for either 90 or 180 days (short-term or long-term respectively). The dose was selected based on previous work where pharmacokinetics showed that netoglitazone crossed the blood-brain barrier after oral administration (15 mg/Kg) and could be detected in micro dialysate from fraction 30-60 min post administration [82]. Control mice were treated with PBS (PBS and condensed milk). The starting age of the treated mice were 56 ± 4 days (Fig. 2a). For whole-brain analysis of Aβ plaques, the protocol was performed as previously described [60]. Briefly: after treatments were completed, mice were deeply anaesthetized with ketamine and xylazine and transcardially perfused first with ice cold PBS, followed by a hydrogel monomer mixture of 4% acrylamide,0.05% bisacrylamide, and 1% paraformaldehyde. Brains were harvested, post incubated in hydrogel mixture overnight and further cleared. For whole-hemisphere analysis of microglia, 2D immunofluorescence (IF), 2D immunohistochemistry (IHC), and RNA sequencing (RNAseq) analysis: mice were deeply anaesthetized with ketamine and xylazine and transcardially perfused first with ice cold PBS, followed by 4% paraformaldehyde. Brains were harvested, and the hemispheres were separated. Left hemispheres were further incubated in the paraformaldehyde solution for 24 hours, then moved to 30% sucrose in PBS for two days at 4 °C and finally they were embedded in paraffin to be further used for whole-

hemisphere analysis of microglia, IF, and IHC. Right hemispheres were snap-frozen right after harvesting and stored at -80 °C.

Behavioral studies

Groups of 10 APPPS1 [32] mice and wild-type (WT) mice treated for 180 days with high-dose of netoglitazone (10 mice per group) and respective controls (PBS) were tested approximately 3-4 days prior perfusion for the following behavioral paradigms:

Light/dark box (LDB) test

The LDB test was used to measure anxiety-like behavior in mice [83]. The LDB consists of four identical two-way shuttle boxes (30 x 30 x 24 cm; Multi Conditioning System, TSE Systems GmbH, Bad-Homburg, Germany). The boxes are each separated by dark plexiglass walls, which are interconnected by an opening (3.5 × 10 cm) in the partition wall, thus allowing the animal to freely traverse from one compartment to the other. This wall divides the compartment into a dark (1 lux) and a brightly illuminated (100 lux) compartment. Mice were individually placed in the center of the dark compartment and were allowed to move freely for 10 min. The distance moved in the light compartment was assessed as an index of innate anxiety in mice [84] (Figure 1C).

Spatial recognition memory

Spatial recognition memory is evaluated by a spatial novelty preference task in the Y-maze [85]. The apparatus was made of transparent Plexiglas and consists of three identical arms (50 × 9 cm; length × width) surrounded by 10-cm high transparent Plexiglas walls. The three arms radiated from a central triangle (8 cm on each side) and were spaced 120° from each other. Access to each arm from the central area can be blocked by a removable opaque barrier wall. The maze was elevated 90 cm above the floor and positioned in a well-lit room enriched with distal spatial cues. For each retention interval to be tested (see below), the experiment was performed in a different room with a distinct set of extra-maze cues surrounding the Y-maze, to avoid confounds by familiar visual cues. A digital camera was mounted above the Y-maze apparatus. Images were captured at a rate of 5 Hz and transmitted to a PC running the EthoVision tracking system (Noldus Information Technology), calculating the time spent and distance moved in the three arms and center zone of the Y-maze. The test of spatial recognition memory in the Y-maze consisted of two phases, called the sample and choice phases. The allocation of arms (start, familiar and novel arm) to a specific spatial location is counterbalanced across the subjects.

• Sample phase: The animals were allowed to explore two arms (referred to as ‘start arm’ and ‘familiar arm’). Access to the remaining arm (‘novel arm’) was blocked by a barrier wall door.

To begin a trial, the animal was introduced at the end of the start arm and allowed to freely explore both the start and the familiar arms for 5 min. The animals were then removed and kept in a holding cage during the specific retention intervals (see below) prior to the choice phase. The barrier door was removed and the floor was cleaned to avoid olfactory cues.

• Choice phase: Following a specific retention interval (see below), the test animal was introduced to the maze again. During the choice phase, the barrier wall was removed so that the animals could freely explore all arms of the maze for 5 min. The subject was then removed from the maze and returned to the home cage. For each trial, the time spent in each of the three arms was recorded. The relative time spent in the novel arm during the choice phase was calculated by the formula ([time spent in the novel arm/[time spent in all arms]) × 100 and used as the index for spatial novelty preference. In addition, total distance moved on the entire maze was recorded and analyzed in order to assess general locomotor activity. To manipulate the retention demand in the temporal domain, the interval between the two phases (i.e. sample and choice phases) of the Y-maze test was varied. First, a minimal interval of 1 min was used. The interval between the two phases was then increased to 2h (Supplementary Figure 1A, 1B).

Open field exploration test

The open field paradigm was used to study of basal locomotor activity [86]. The open field exploration test was conducted in four identical square arenas (40×40×35 cm high) made of opaque acryl glass. They were located in a testing room under diffused lighting (approximately 25 lx as measured in the center of the arenas). A digital camera was mounted directly above the four arenas. Images were captured at a rate of 5 Hz and transmitted to a PC running the Ethovision (Noldus, The Netherlands) tracking system. For measuring basal locomotor activity, the animals were gently placed in the center of the arena and allowed to explore for 10 min. Distance moved in the entire arena was assessed to index locomotor activity (Supplementary Figure 1C).

Temporal order memory test

A temporal order memory test was used as a test for prefrontal cortex-dependent short-term memory. The mouse was first subjected to a training trial, where it was placed in an open field (square arena 40×40×35 cm high) with two copies of a novel object and allowed to explore them for 10 min. After the 10 min exploration, the mouse was placed back into a waiting cage. After a delay of 60 min, the mouse received a second training trial identical to the first, except that two copies of a new novel object will be present. Again, after the second training trial the mouse was placed back into the waiting cage. After a further delay of either 2 h or no delay, the mouse received a test trial identical to the training trials, except that one copy of the object

from trial 1 (the old familiar object) and one copy of the object from trial 2 (the recent familiar object) were presented. For each animal, a temporal order memory index was calculated by the formula: ([time spent with phase 1 object] / [time spent with phase 1 object + time spent with phase 2 object]) * 100. The temporal order memory index was used to compare the animals' capacity to discriminate the relative regency of stimuli [87], with values > 50 signifying a capacity to discriminate between the temporally more remote object presented in sample phase 1 and the temporally more recent object presented in sample phase 2. In addition, the relative amount of time exploring the objects in sample phases 1 and 2 of the test were analyzed to measure object exploration per se (Figure 2E).

Contextual Fear Conditioning

Contextual fear conditioning and extinction were conducted using 4 identical multi-conditioning chambers (Multi Conditioning System, TSE Systems, Bad Homburg, Germany), in which the animals were confined to a rectangular enclosure (30 [length] × 30 [width] × 36 [height] cm) made of black acrylic glass. The chambers were equivalently illuminated by a red house light (30 lux) and were equipped with a grid floor made of 29 stainless rods (4 mm in diameter and 10 mm apart; inter-rod center to inter-rod center), through which a scrambled electric shock could be delivered. Each chamber was surrounded by 3 infrared light-beam sensor systems, with sensors spaced 14 mm apart, allowing movement detection in 3 dimensions. The contextual fear conditioning and extinction test followed protocols established before [33, 88] and consistent of 3 phases, which were each separated 24h apart (see below). During all three phases, the red house light was on at all times. Conditioned fear was expressed as freezing behavior, which was quantified automatically by program-guided algorithms as time of immobility. Habituation and conditioning phase: The animals were placed in the designated test chamber and were allowed to freely explore the chamber for 3 min. This served to habituate the animals to the chamber. Conditioning commenced immediately at the end of the habituation period without the animals being removed from the chambers. For conditioning, the animals were exposed to 3 conditioning trials, whereby each conditioning trial began with the delivery of a 1 second foot-shock set at 0.3 mA and was followed by a 90s rest period. The animals were removed from the chambers and were placed back in their home cages immediately after the last trial. Fear expression phase: The fear expression phase took place 24h and 48h after conditioning when the animals were returned to the same chambers in the absence of any discrete stimulus other than the context. To assess conditioned fear towards to the context, percent time freezing was measured for a period of 6 min. The animals were then removed from the boxes and placed back to their home cages (Figure 2C).

Tissue clearing and staining of Aβ plaques with focused electrophoretic tissue

For whole-brain analysis of Aβ plaques, brains were cleared with focused electrophoretic tissue clearing (FEC) in accordance to [60]. Briefly: Brains were placed in a custom-built chamber in 8% clearing solution (8% w/w sodium dodecyl sulphate in 200 mM boric acid, pH 8.5) and cleared for approximately 16h at 130 mA current-clamped and at a voltage limit of 60V, at 39.5 °C. Transparency was assessed by visual inspection. Immunofluorescence staining of Aβ plaques was performed in accordance to the protocol described in [60]. Briefly: amyloid plaques were stained with a combination of luminescent conjugated polythiophenes (LCPs), heptamer-formyl thiophene acetic acid (hFTAA), and quadro-formyl thiophene acetic acid (qFTAA). The combination of these dyes was used for the discrimination of neuritic plaques at different maturation states [89]. After staining brains were refractive index (RI) - matched to 1.46 with a modified version of the refractive index matching solution [90] by including triethanolamine [60] (Supplementary Figure 3).

Whole-brain imaging of Aβ plaques

Whole brain images were recorded with a custom-made selective plane illumination microscope (www.mesospim.org) [36]. SPIM imaging was done after clearing and refractive index matching as previously described in [60]. Briefly: the laser/filter combinations for mesoSPIM imaging were as follows: for qFTAA at 488 nm excitation, a 498 - 520 nm bandpass filter (BrightLine 509/22 HC, Semrock / AHF) was used as the emission filter; for hFTAA at 488 nm excitation, a 565 - 605 nm bandpass filter (585/40 BrightLine HC , Semrock / AHF) was used. Transparent whole-brains were imaged at a voxel size of 3.26 × 3.26 × 3 μm^3 (X × Y × Z). For scanning a whole brain, 16 tiles per channel were imaged (8 tiles per brain hemisphere). After the acquisition of one hemisphere, the sample was rotated and the other hemisphere was then acquired. The entire process was followed by stitching [91] (Supplementary Figure 3).

Tissue clearing and whole-hemisphere staining of microglia with DISCO

Mouse hemispheres were stained for microglia using a modified version of the iDISCO protocol [39]. Deparaffination was performed using a custom-developed protocol as part of the aDISCO protocol (unpublished). Paraffin-embedded mouse hemispheres were melted for 1 hour at 60°C, followed by incubation in xylene for 1 hour at 37°C and 65 rpm and for 1 hour at room temperature (RT) and 40 rpm. Rehydration was performed by serial incubations of 100%, 95%, 90%, 80%, 70%, 50%, and 25% ethanol (EtOH) in ddH_2O, followed by incubation

in PBS overnight at RT and 40 rpm. Samples were again dehydrated in serial incubations of 20%, 40%, 60%, 80% methanol (MeOH) in ddH_2O, followed by 2 times 100% MeOH, each for 1 hour at RT and 40 rpm. Pre-clearing was performed in 33% MeOH in dichloromethane (DCM) overnight at RT and 40 rpm. After 2 times washing in 100% MeOH each for 1 hour at RT and then 4°C at 40 rpm, bleaching was performed in 5% hydrogen peroxide in MeOH for 20 hours at 4°C and 40 rpm. Samples were rehydrated in serial incubations of 80%, 60%, 40%, and 20% MeOH in in ddH_2O, followed by PBS, each for 1 hour at RT and 40 rpm. Permeabilization was performed by incubating the mouse hemispheres 2 times in 0.2% TritonX-100 in PBS each for 1 hour at RT and 40 rpm, followed by incubation in 0.2% TritonX-100 + 10% dimethyl sulfoxide (DMSO) + 2.3% glycine + 0.1% sodium azide (NaN3) in PBS for 5 days at 37°C and 65 rpm. Blocking was performed in 0.2% Tween-20 + 0.1% heparin (10 mg/ml) + 5% DMSO + 6% donkey serum in PBS for 2 days at 37°C and 65 rpm. Samples were stained gradually with primary polyclonal rabbit-anti-Iba1 antibody (Wako, 019-19741) 1:400, followed by secondary polyclonal 647-conjugated donkey-anti-rabbit antibody (ThermoFisher, A-31573) in 0.2% Tween-20 + 0.1% heparin + 5% DMSO + 0.1% NaN3 in PBS (staining buffer) in a total volume of 1.5 ml per sample every week for 2 weeks at 37°C and 65 rpm. Washing steps were performed in staining buffer 5 times each for 1 hour, and then for 1-2 days at RT and 40 rpm. Clearing was started by dehydrating the samples in serial MeOH incubations as described above. Delipidation was performed in 33% MeOH in DCM overnight at RT and 40 rpm, followed by 2 times 100% DCM each for 20 minutes at RT and 40 rpm. Refractive index (RI) matching was achieved in dibenzyl ether (DBE, RI = 1.56) for 4 hours at RT. 3D stacks of cleared mouse hemispheres were acquired using the mesoSPIM light-sheet microscope [36] (www.mesospim.org) at 2X zoom with a field of view of 1.3 cm and isotropic resolution of 3 µm/voxel. To image the microglia a 640nm laser and a F76 647SG long pass filter were used. Imaged tiles were stitched together [91] and raw data were post-processed using Fiji (Image J, 1.8.0_172 64 bit) and Imaris (Oxford Instruments, 9.8.0) (Supplementary Figure 3).

2D immunofluorescence staining of Aβ plaques with antibody

Slices from formalin fixed and paraffin embedded brain tissue from 180 day-treated APPPS1 mice (n=3) were stained for Aβ plaques. Slices were stained with mouse anti-human $Aβ_{1-16}$ antibody (6E10, Biolegend SIG-39320, 1:200) after antigen retrieval with 10% formic acid. Slices were blocked with M.O.M. Kit (BMK-2202) and the primary antibody was detected with Alexa-488 conjugated goat anti-mouse IgG (Invitrogen A-11005, 1:1000 dilution) followed by diamidino-phenylindole (DAPI) staining. Slices were imaged with a Leica SP5 confocal microscope. Nuclei and plaques were imaged with a 10X/0.25 (numerical aperture 0.4). NA

dry objective, using the following settings: 405 nm excitation for DAPI (nuclei) and 488nm excitation for amyloid. The dynamic range of images was adjusted consistently across images. Three different cortical regions and one thalamic region were selected per slice (2 slices per sample). Pixels representing the region of interest were classified and counted as plaques (6E10-Alexa488 positive) or background (6E10-Alexa488 negative) with a manually trained (trained on ten images) pixel classifier in ILASTIK [38], and ImageJ. Hypothesis testing was done with a 2-tailed T-test (Supplementary Figure 4B).

2D immunohistochemistry staining of Aβ plaques with antibody

Slices from formalin fixed and paraffin embedded brain tissue from 180 day-treated APPPS1 mice (n=3) were stained for Aβ plaques. 6-µm-thick paraffin sections (3 sections per mouse) were deparaffinized through a decreasing alcohol series. Slices were stained with Slices were stained with mouse anti-human $A\beta_{1\text{-}16}$ antibody (6E10, Biolegend SIG-39320, 1:200) and detected using an IVIEW DAB Detection Kit (Ventana). Sections were imaged using a Zeiss Axiophot light microscope. For the quantification of plaque staining in the whole section, pixels were classified and counted as plaques (Aβ positive) or background (Aβ negative) with a manually trained (trained on five images) pixel classifier in ILASTIK [92], and ImageJ. Hypothesis testing was done with a 2-tailed T-test (Supplementary Figure 4A).

Drug distribution measurements in plasma

7 days and 28 days post dosing, serial blood samples (~50µL) were taken from the tail vein of individual animals and delivered into labelled Safe-lock Eppendorf 1.5 mL clear (e.g. T9661 Sigma Aldrich) containing Na-heparin as the anticoagulant (1000iU, 2µL per vial). The samples was held on wet ice for a maximum of 30 minutes while sampling of all the animals in the cohort was completed. The blood samples were centrifuged for plasma (4°C, 2000-3000g for 8 min) and 25µL of the resulting plasma were analyzed. Drug concentration in plasma was calculated by Parmidex, London, UK (Figure 1B).

Computational and statistical analysis for whole-brain Aβ quantification

The following computations were performed using custom scripts written in Python and R [93] as well as existing third-party libraries as previously described[60]. Briefly, the 2-channel (498–520 nm and 565-605 nm) sub-stacks for each brain hemisphere were first stitched together with TeraStitcher [91]. The result was down sampled from the acquired resolution (3.26 µm lateral, 3 µm depth) to an isotropic 25 µm resolution and then registered to the Allen Brain

673 Atlas 25 μm average anatomical template atlas [40]. The 565-605 nm channel at its original
674 resolution was used to determine the locations of aggregates of amyloid-β stained with qFTAA
675 and hFTAA. A random forest classifier was used to classify each voxel as either “belonging to
676 a plaque” or “background” using the open-source Ilastik framework [92] as described in [60].
677 After down-sampling each aggregate center to 25-μm resolution and applying the optimized
678 registration transformation, the number of aggregates were counted at each voxel in this atlas
679 space and smoothed heatmaps were generated by placing a spherical ROI with 15-voxel
680 diameter (= 375μm) at each voxel and summing the plaque counts within the ROI, as
681 described in [60] (Supplementary Figure 3A, 3B).

682 Voxel-level statistics across treated and control brains involved running a two-sided t-test at
683 each heatmap voxel across the two groups. The three-dimensional statistical maps were
684 adjusted using the threshold-free cluster enhancement method [94]. These adjusted p-value
685 maps were then binarized with a threshold of 0.05 for subsequent analysis or visualization.
686 The transformed locations of each plaque were further grouped into 52 different anatomically
687 segmented regions in the Allen Reference Atlas (25) for further statistical analysis between
688 longitudinal groups. These anatomical regions were masked to only include voxels that
689 demonstrated a statistically significant difference ($p < 0.05$).

690

691 *Computational and statistical analysis for whole-hemisphere microglia quantification*

692 The 640 nm channel in its original resolution was used to determine the spatial density of
693 microglia and all the substacks for each brain hemisphere were first stitched together with
694 Terastitcher [91]. Advanced filtering techniques implemented in Python and C were used
695 within a custom pipeline, available on github (https://github.com/aecon/3D-microglia-
696 netoglitazone), aimed at high-speed processing of 3D half-brain mouse datasets. The pipeline
697 consists of three main steps: (i) image restoration, (ii) voxel-based microglia detection, and
698 (iii) regional microglia-density quantification. First, image restoration was performed to
699 alleviate low frequency background (autofluorescence) undulations, and remove high
700 frequency noise at the voxel level introduced during the digitization of the image via the
701 microscope camera [95]. Specifically, background intensity is modelled via Gaussian
702 smoothing of the raw data. The variance is set to 50 voxels, such that it is larger than the
703 typical foreground (microglia) radius, but smaller than the typical radius of background regions
704 with high autofluorescence. The background undulations are removed by dividing the raw data
705 with the smoothed data [96], yielding the normalized data. Lastly, digitization noise is
706 suppressed via a Gaussian smoothing of the normalized image with a small variance of 1
707 voxel, modelling the intervoxel noise. Microglia detection was performed by applying a

minimum threshold on the normalized intensity data. The threshold was set to 1.8 for all samples, chosen such that large and bright microglia are detected, while at the same time noise and regions of high tissue autofluorescence are excluded. This leads to the binarized data where each pixel is classified as background or foreground. Connected foreground voxels are identified as single microglia cells, and thresholds on the minimum possible microglia volume and minimum maximum microglia intensity are applied to eliminate smaller and/or dimmer artifacts. The segmentation results for all 9 samples were validated by a domain expert, through a visual inspection of the detected microglia overlayed on the raw data (Supplementary Figure 5).

Spatial distribution of microglia volume was then estimated by mapping the detected microglia on the Allen Reference Atlas. This step was achieved using elastix [97] where the autofluorescence from the plaque channel (565-605 nm) was first down-sampled to the atlas resolution (25 μm per voxel side) and then used to spatially transform the autofluorescence data such that they match the atlas geometry. This process gave an optimized registration transformation per sample. The optimized transformation was then applied on the detected microglia voxels, after down-sampling to the atlas resolution. Assuming that the density is constant over all selected microglia voxels, the total microglia volume per atlas voxel was computed by counting the number of microglia voxels mapped onto each atlas voxel. The quantification of microglia distribution was performed using density plots, depicting the volume of detected microglia inside a cubic pixel with the atlas resolution. Similar to the plaque quantification, smoothed heatmaps were generated by placing a spherical ROI with 15-voxel diameter and taking a weighted sum of the microglia volume within the ROI. Coronal sections of the volume distribution for every sample, were overlayed on the respective slices of the Allen Brain Atlas (Fig. 5a). The average microglia volume distribution per group was computed by taking the mean over the samples belonging to each group (Fig. 5b). Using the 134 different anatomically segmented regions of the Allen Reference Atlas, the anatomical regions of the detected microglia were identified, and the total volume in six brain regions was computed: brain stem, hippocampus, hypothalamus, cortex, thalamus, cerebellum. The group-wise average microglia volume and corresponding standard deviation per brain region were then computed. To measure the degree of spatial colocalization between microglia cell count change and plaque count change following long-term treatments of either low or high dose drug, thresholded voxel level statistical maps ($p < 0.05$, corrected) for each group were first generated in the Allen Coordinate Space. To compare two statistical maps from different groups, we calculate the number of overlapping voxels between the significantly increasing, or decreasing, parts of the first map with the significantly increasing, or decreasing, parts of another map. This results in four distinct

comparisons, and a colocalization matrix as depicted in Figure 4B. This analysis was performed for comparing the changes in microglia cell count with plaque changes in the low dose (long-term) treatment group, and separately for comparing the changes in microglia cell count with plaque changes in the high dose (long-term) treatment group.

RNA sequencing

Group of treated and controls APPPS1 mice (7 high-dose, low-dose and 7 PBS-treated mice) were analyzed for transcriptomic changes. Snap-frozen hemispheres were sectioned in slices of 10 µm, and total RNA was extracted by following a standard RNA extraction protocol (TRIzol Reagent Ref. 15596026). The RNA quality and quantity were assessed using a spectrophotometer, and only high-quality RNA samples were used for subsequent RNA-seq library preparation. The RNA-seq libraries were prepared using a library preparation kit compatible with the sequencing platform (Nova Seq Illumina Library) following the manufacturer's instructions. Subsequently, the libraries were sequenced on a high-throughput sequencing instrument, generating millions of reads per sample.

Post-processed DEGs were visualized with volcano plot showing statistical significance (P-value) versus magnitude of change (fold change). Statistical threshold has been applied prior data visualization (absolute log2 fold change > 0.5 and pvalue < 0.005). Customized script was used to generate the related plot by using R and RStudio platform. For data wrangling, the tidyverse, tidyr and dyplr R packages have been used, while for data visualization ggplot2 and ggpubr packages were used. Differential downregulated genes are shown in green, whereas upregulated genes in magenta.

Acknowledgments

We thank Wren Therapeutics, Cambridge, UK, for providing netoglitazone.

Funding

A.A. is supported by institutional core funding by the University of Zurich and the University Hospital of Zurich, a Distinguished Scientist Award of the NOMIS Foundation, and grants from the GELU Foundation, the Swiss National Science Foundation (SNSF grant ID 179040 and grant ID 207872, Sinergia grant ID 183563), the HMZ ImmunoTarget grant, the Human Frontiers Science Program (grant ID RGP0001/2022), and the Michael J. Fox Foundation (grant ID MJFF-022156). JHL is supported by NIH/NINDS DP1 NS116783; NIH/NINDS R01 AG064051; NIH/NINDS R01 EB030884. SL, is supported by the European High Performance Computing Joint Undertaking (EuroHPC) Grant DComEX (956201-H2020-JTI-EuroHPC-2019-1).

Figures and Figure legends

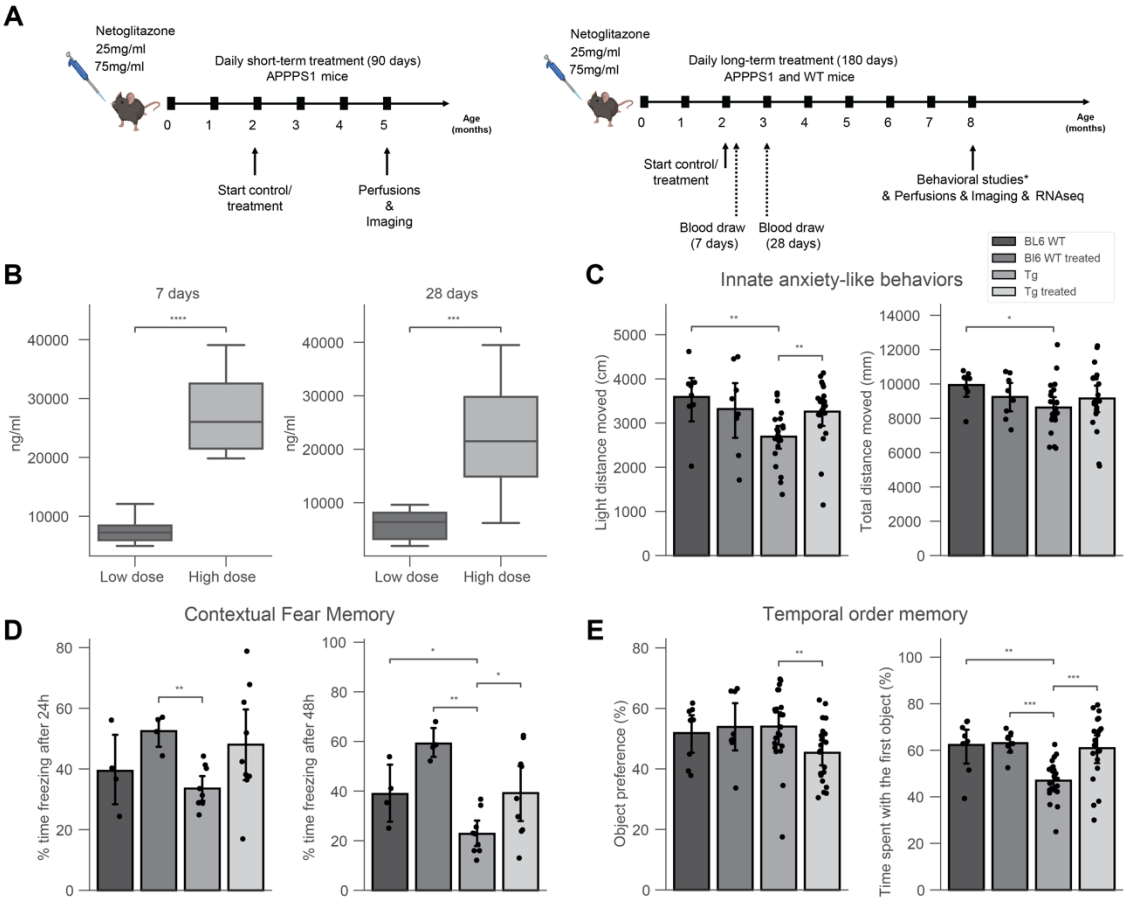

Figure 1: 180 days of treatment with netoglitazone induces anxiolytic-like effects, alters fear memory and restores deficit in temporal order memory in AD mice. (A) APPPS1 mice were treated daily with either a high dose (75 mg/ml) or a low dose (15 mg/ml) of netoglitazone or appropriate control (PBS). Treatment started at 2 months of age and continued for either three or six months. Mice were perfused and brains were further analyzed at either five or eight months of age. Behavioral studies and RNAseq analysis were performed only on mice treaded for 180 days with a high dose of netoglitazone. (B) Blood was withdrawn from mice of the long-term treatment cohort seven and twenty-eight days after the start of the treatment. Drug concentration was measured in the plasma. Plasma drug concentration increased in line with time in both dosing cohorts. (C) Behavioral tests: Drug treatment induced anxiolytic-like effects in Tg animals, as indexed by an increased distance moved in the light compartment when compared to untreated Tg animals, as well as to wild type (WT) animals, without affecting general maze exploration. (D) Contextual fear memory: In male mice, long-term drug treatment enhanced expression of contextual fear independent of the genotype after 24h. After 48h, transgenic (Tg) mice displayed a reduction in fear memory, with a treatment-

823 dependent increase, independent of genotype. (E) Tg animals displayed a deficit in temporal
824 order memory, which was restored to control levels by the drug treatment. This was not
825 confounded by changes in the preference towards one of the distinct sets of objects.

826

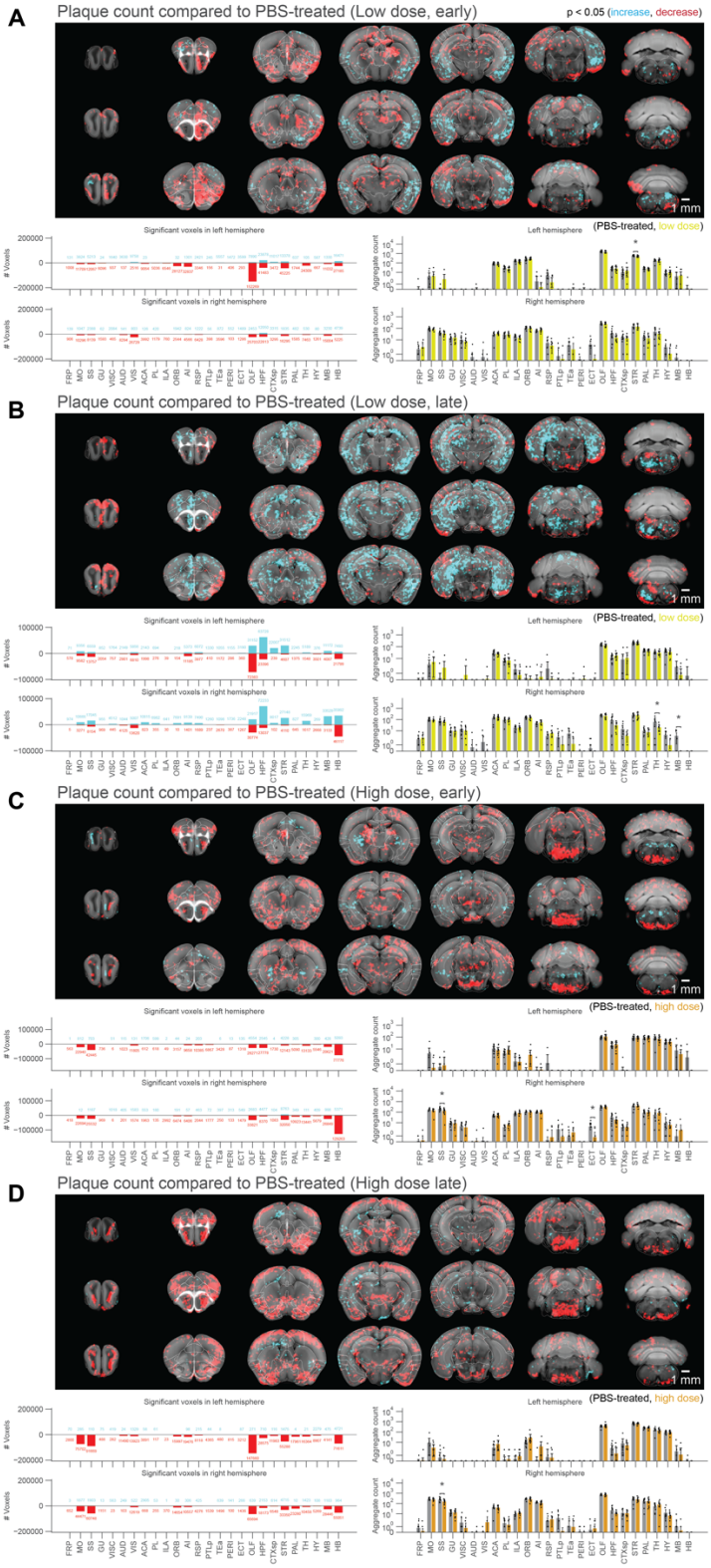

827

828 **Figure 2: Voxel-based whole-brain analysis shows regional and dose-dependent effects**
829 **of netoglitazone in decreasing plaque count.** The figure presents a series of maps and
830 plots illustrating the effects of different treatments on plaque count. Each map represents a 3-
831 dimensional view of statistically affected voxels (p<0.05), where the red scale indicates a

decrease in plaque count, and the cyan scale represents an increase. The reference atlas is depicted in grey. The maps provide a comprehensive summary of treated and control samples within each cohort, with 6-8 samples per group. Additionally, the plots on the right side display the average plaque count across the cohorts. The figure highlights the regiospecific efficacy unique to each treatment modality: (A) Short-treatment with a low dose of netoglitazone shows a patchy effect in reducing plaque count, primarily observed in the olfactory, striatal, and thalamic areas. (B) Long-term-treatment with a low dose of netoglitazone also exhibits a patchy effect in decreasing plaque count. This effect is mainly observed in the olfactory, hindbrain, and visual areas. Notably, there is a patchy increase in plaque count observed in the hippocampal, cortical, striatal, and midbrain areas. (C) Short-treatment with a high dose of netoglitazone reveals a significant reduction in plaque count, particularly in the hindbrain, midbrain, striatum, and olfactory areas. (D) Long-term treatment with a high dose of netoglitazone demonstrates a considerable decrease in plaque count, especially in the olfactory, striatum, pallidum, hindbrain, and midbrain regions.

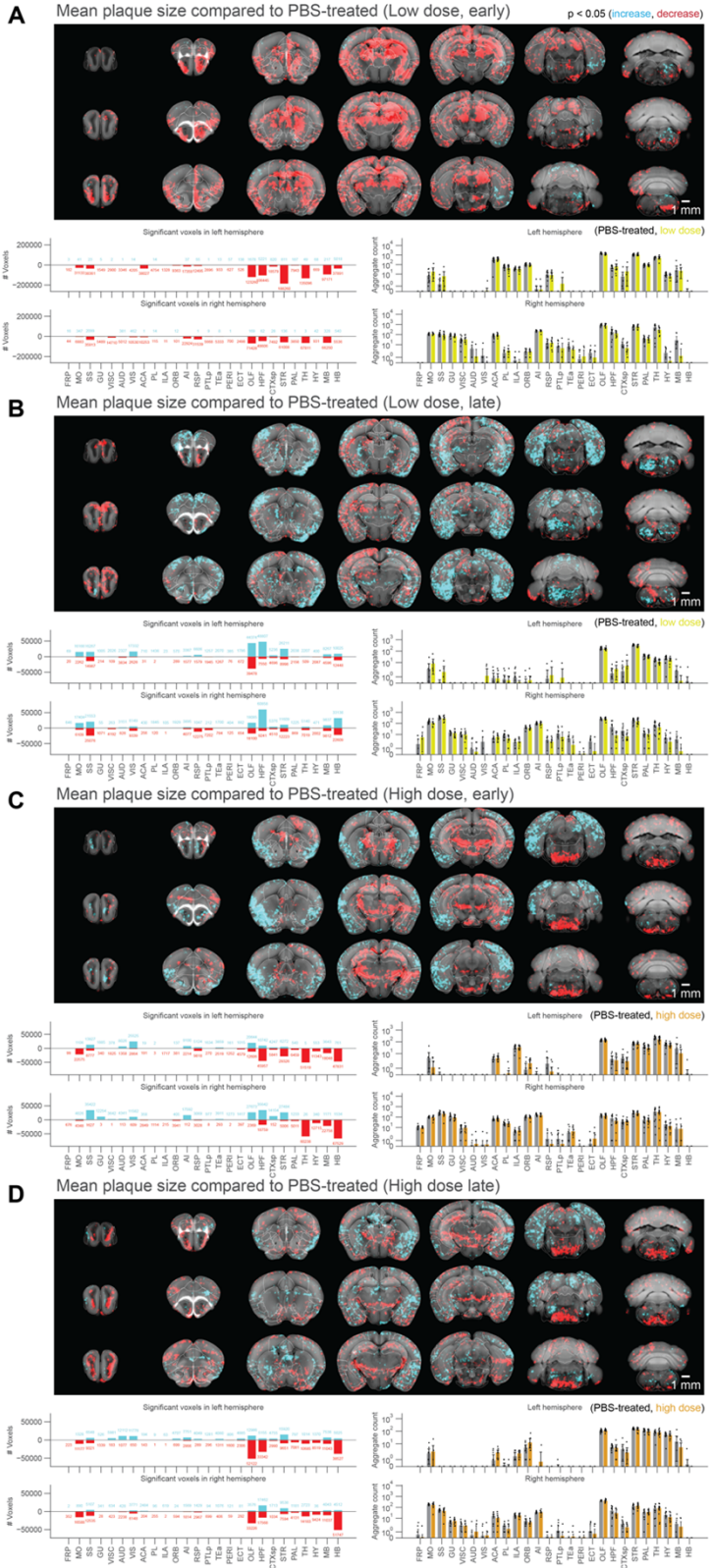

Figure 3: Voxel-based whole-brain analysis shows regional and dose-dependent effects of netoglitazone in decreasing plaque mean size. The figure presents a series of maps and plots illustrating the effects of different treatments on plaque size. Each map represents a 3-

dimensional view of statistically affected voxels ($p<0.05$), where the red scale indicates a decrease in plaque size, and the cyan scale represents an increase. The reference atlas is depicted in grey. The maps provide a comprehensive summary of treated and control samples within each cohort, with 6-8 samples per group. Additionally, the plots on the right side display the average plaque count across the cohorts. The figure highlights the regiospecific efficacy unique to each treatment modality: (A) Short-treatment with a low dose of netoglitazone displays a notable patchy effect in reducing plaque size, primarily observed in the olfactory, hippocampal, striatal, thalamic, and midbrain areas. (B) Long-term-treatment with a low dose of netoglitazone demonstrates a patchy effect primarily in increasing plaque size, mainly observed in the optical cortex, visual area, hippocampus, striatum, and hindbrain. However, there is only a minimal effect on decreasing plaque size. (C) Short-treatment with a high dose of netoglitazone reveals a significant reduction in plaque size, especially observed in the hippocampus, striatum, thalamus, hypothalamus, midbrain, and hindbrain. Additionally, there is an increase in plaque size mainly observed in the olfactory, hippocampal, cortical, and striatal areas. (D) Long-term treatment with a high dose of netoglitazone displays a decrease in plaque size, particularly observed in the orbital cortex, olfactory area, hippocampus, thalamus, hypothalamus, midbrain, and hindbrain regions.

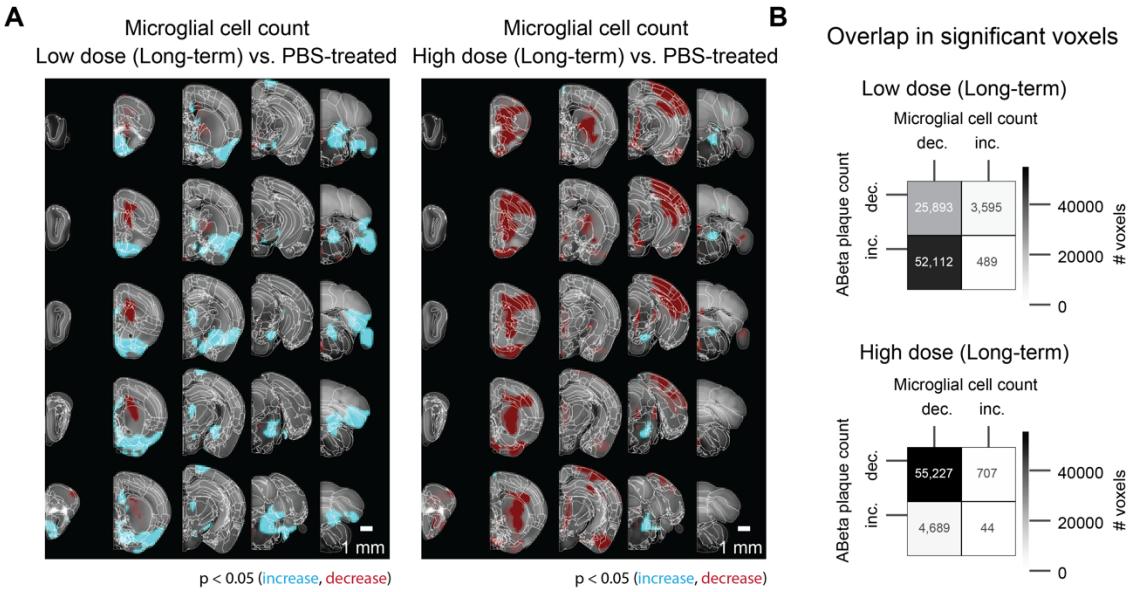

Figure 4: Voxel-based whole-hemisphere analysis shows regional and dose-dependent decrease of microglia. (A) Each 3-dimensional map of statistically affected voxels ($p < 0.05$, with the red scale, representing the significance in decrease of microglia, and the cyan scale, representing the increase in microglia; reference atlas is grey) summarizes all the treated and control samples within a cohort (3 samples per group). These maps illustrate that the effectiveness of reducing microglia is specific to particular regions and varies based on the dosage of the treatment. When netoglitazone is administered in low doses over long-term treatment, it only has a limited impact on reducing the overall volume of microglia. However, when high doses of netoglitazone are administered for long-term, it produces a significant and scattered effect, leading to a noticeable reduction in microglia volume in cortical and hippocampal regions. (B) Colocalizing a microglia statistical map with an Aβ plaque statistical maps allows for calculations of the number of overlapping voxels with statistically significant increase or decrease across the two maps. For the late low dose treatment, an increase in Aβ plaque count was colocalized with decreased microglia. For the late high dose treatment, the decrease in Aβ plaque count was also colocalized with decreased microglia.

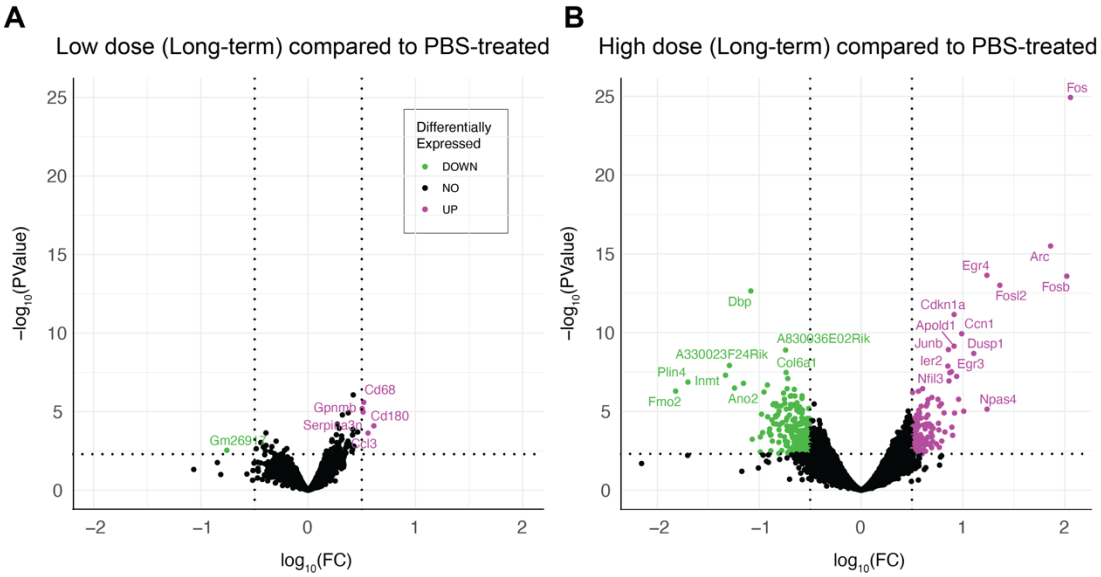

Figure 5: Gene expression changes are revealed by RNAseq upon long-term treatment with netoglitazone. (A) Volcano plots depicting the gene regulation effects of long-term treatment with netoglitazone at different doses. The plots include genes that exhibit significant regulation, determined using thresholds of abs|$\log_2$FC| > 0.5 and p-value < 0.005. The volcano plot for long-term treatment with a low dose of netoglitazone illustrates the significantly regulated genes. Upregulated genes are represented in magenta, while downregulated genes are shown in green. In comparison to the PBS group, animals treated with a low dose of netoglitazone display a notable number of both downregulated and upregulated differentially expressed genes (DEGs). (B) The volcano plot for long-term treatment with a high dose of netoglitazone depicts the significantly regulated genes. Similar to the previous plot, upregulated genes are indicated in magenta, while downregulated genes are displayed in green. However, in contrast to the low dose treatment, animals treated with a high dose of netoglitazone exhibit a minimal number of both downregulated and upregulated DEGs compared to the PBS group.

References

1. *2020 Alzheimer's disease facts and figures.* 2020. **16**(3): p. 391-460.
2. Ashraf, G.M., et al., *Protein misfolding and aggregation in Alzheimer's disease and type 2 diabetes mellitus.* CNS Neurol Disord Drug Targets, 2014. **13**(7): p. 1280-93.
3. Bloom, G.S., *Amyloid-β and tau: the trigger and bullet in Alzheimer disease pathogenesis.* JAMA Neurol, 2014. **71**(4): p. 505-8.
4. Hensley, K., et al., *A model for beta-amyloid aggregation and neurotoxicity based on free radical generation by the peptide: relevance to Alzheimer disease.* Proc Natl Acad Sci U S A, 1994. **91**(8): p. 3270-4.

5. Hardy, J.A. and G.A. Higgins, *Alzheimer's disease: the amyloid cascade hypothesis.* Science, 1992. **256**(5054): p. 184-5.
6. Morris, G.P., I.A. Clark, and B. Vissel, *Inconsistencies and Controversies Surrounding the Amyloid Hypothesis of Alzheimer's Disease.* Acta Neuropathologica Communications, 2014. **2**(1): p. 135.
7. Serrano-Pozo, A., et al., *Neuropathological alterations in Alzheimer disease.* Cold Spring Harb Perspect Med, 2011. **1**(1): p. a006189.
8. Sevigny, J., et al., *The antibody aducanumab reduces Aβ plaques in Alzheimer's disease.* Nature, 2016. **537**(7618): p. 50-6.
9. Holtzman, D.M., J.C. Morris, and A.M. Goate, *Alzheimer's disease: the challenge of the second century.* Sci Transl Med, 2011. **3**(77): p. 77sr1.
10. Cummings, J., et al., *Alzheimer's disease drug development pipeline: 2019.* Alzheimers Dement (N Y), 2019. **5**: p. 272-293.
11. Piazza, F., et al., *Anti-amyloid β autoantibodies in cerebral amyloid angiopathy-related inflammation: implications for amyloid-modifying therapies.* Ann Neurol, 2013. **73**(4): p. 449-58.
12. Adhikari, U.K., et al., *Therapeutic anti-amyloid β antibodies cause neuronal disturbances.* Alzheimers Dement, 2022.
13. van Dyck, C.H., et al., *Lecanemab in Early Alzheimer's Disease.* N Engl J Med, 2023. **388**(1): p. 9-21.
14. Wang, Y., *An insider's perspective on FDA approval of aducanumab.* Alzheimer's & Dementia: Translational Research & Clinical Interventions, 2023. **9**(2): p. e12382.
15. Knopman, D.S., D.T. Jones, and M.D. Greicius, *Failure to demonstrate efficacy of aducanumab: An analysis of the EMERGE and ENGAGE trials as reported by Biogen, December 2019.* Alzheimer's & Dementia, 2021. **17**(4): p. 696-701.
16. Sims, J.R., et al., *Donanemab in Early Symptomatic Alzheimer Disease: The TRAILBLAZER-ALZ 2 Randomized Clinical Trial.* Jama, 2023. **330**(6): p. 512-527.
17. *The Human Protein Atlas*.
18. Hu, W., et al., *Expression of Tau Pathology-Related Proteins in Different Brain Regions: A Molecular Basis of Tau Pathogenesis.* Front Aging Neurosci, 2017. **9**: p. 311.
19. *The Human Protein Atlas*.
20. Suzuki, T., et al., *Regional and cellular presenilin 1 gene expression in human and rat tissues.* Biochem Biophys Res Commun, 1996. **219**(3): p. 708-13.
21. Kirschenbaum, D., et al., *Whole-brain microscopy reveals distinct temporal and spatial efficacy of anti-Aβ therapies.* EMBO Molecular Medicine, 2023. **15**(1): p. e16789.
22. Dubois, B., et al., *Preclinical Alzheimer's disease: Definition, natural history, and diagnostic criteria.* Alzheimers Dement, 2016. **12**(3): p. 292-323.
23. Jack, C.R., Jr., et al., *NIA-AA Research Framework: Toward a biological definition of Alzheimer's disease.* Alzheimers Dement, 2018. **14**(4): p. 535-562.
24. Klunk, W.E., et al., *Imaging brain amyloid in Alzheimer's disease with Pittsburgh Compound-B.* Ann Neurol, 2004. **55**(3): p. 306-19.
25. Thal, D.R., et al., *Phases of Aβ-deposition in the human brain and its relevance for the development of AD.* Neurology, 2002. **58**(12): p. 1791-1800.
26. Schmidt, S.D., R.A. Nixon, and P.M. Mathews, *ELISA method for measurement of amyloid-beta levels.* Methods Mol Biol, 2005. **299**: p. 279-97.
27. Pedrero-Prieto, C.M., et al., *Human amyloid-β enriched extracts: evaluation of in vitro and in vivo internalization and molecular characterization.* Alzheimer's Research & Therapy, 2019. **11**(1): p. 56.
28. Rafii, M.S., & Aisen, P. S., *Brain region-specific pharmacodynamics.* Alzheimer's & Dementia: The Journal of the Alzheimer's Association, 2009.

29. Livingston, G., et al., *Dementia prevention, intervention, and care: 2020 report of the Lancet Commission.* Lancet, 2020. **396**(10248): p. 413-446.
30. Ballard, C., et al., *Drug repositioning and repurposing for Alzheimer disease.* Nat Rev Neurol, 2020. **16**(12): p. 661-673.
31. HABCHI, J.Y., Xiaoting JENKINS, Kerry PERNI, Michele SARWAT, Sunehera MENZIES, Joseph CAMPERO PEREDO, Christina POSSENTI, Andrea LINSE, Sara KNOWLES, Tuomas DOBSON, Christopher COHEN, Samuel VENDRUSCOLO, Michele, *THERAPY FOR PROTEIN MISFOLDING DISEASE,* W.T. LIMITED, Editor. 2019.
32. Radde, R., et al., *Abeta42-driven cerebral amyloidosis in transgenic mice reveals early and robust pathology.* EMBO Rep, 2006. **7**(9): p. 940-6.
33. Labouesse, M.A., W. Langhans, and U. Meyer, *Long-term pathological consequences of prenatal infection: beyond brain disorders.* Am J Physiol Regul Integr Comp Physiol, 2015. **309**(1): p. R1-r12.
34. Kirschenbaum, D., et al., *Whole-brain microscopy reveals distinct temporal and spatial efficacy of anti-Aß therapies.* 2022: p. 2021.01.15.426090.
35. Nilsson, K.P.R., et al., *Structural Typing of Systemic Amyloidoses by Luminescent-Conjugated Polymer Spectroscopy.* The American Journal of Pathology, 2010. **176**(2): p. 563-574.
36. Voigt, F.F., et al., *The mesoSPIM initiative: open-source light-sheet microscopes for imaging cleared tissue.* Nature Methods, 2019. **16**(11): p. 1105-1108.
37. Lein, E.S., et al., *Genome-wide atlas of gene expression in the adult mouse brain.* Nature, 2007. **445**(7124): p. 168-176.
38. *https://www.ilastik.org/*.
39. Renier, N., et al., *iDISCO: a simple, rapid method to immunolabel large tissue samples for volume imaging.* Cell, 2014. **159**(4): p. 896-910.
40. Wang, Q., et al., *The Allen Mouse Brain Common Coordinate Framework: A 3D Reference Atlas.* Cell, 2020. **181**(4): p. 936-953.e20.
41. *Gotta Get Rid of It All: Total Plaque Clearance Key for Clinical Benefit*. 2023; Available from: https://www.alzforum.org/news/conference-coverage/gotta-get-rid-it-all-total-plaque-clearance-key-clinical-benefit.
42. Braissant, O., et al., *Differential expression of peroxisome proliferator-activated receptors (PPARs): tissue distribution of PPAR-alpha, -beta, and -gamma in the adult rat.* Endocrinology, 1996. **137**(1): p. 354-66.
43. Moreno, S., S. Farioli-Vecchioli, and M.P. Cerù, *Immunolocalization of peroxisome proliferator-activated receptors and retinoid X receptors in the adult rat CNS.* Neuroscience, 2004. **123**(1): p. 131-45.
44. Gofflot, F., et al., *Systematic Gene Expression Mapping Clusters Nuclear Receptors According to Their Function in the Brain.* Cell, 2007. **131**(2): p. 405-418.
45. Sarruf, D.A., et al., *Expression of peroxisome proliferator-activated receptor-gamma in key neuronal subsets regulating glucose metabolism and energy homeostasis.* Endocrinology, 2009. **150**(2): p. 707-12.
46. Morales-Garcia, J.A., et al., *Phosphodiesterase 7 inhibition preserves dopaminergic neurons in cellular and rodent models of Parkinson disease.* PLoS One, 2011. **6**(2): p. e17240.
47. Galimberti, D. and E. Scarpini, *Pioglitazone for the treatment of Alzheimer's disease.* Expert Opin Investig Drugs, 2017. **26**(1): p. 97-101.
48. Villapol, S., *Roles of Peroxisome Proliferator-Activated Receptor Gamma on Brain and Peripheral Inflammation.* Cell Mol Neurobiol, 2018. **38**(1): p. 121-132.
49. Sastre, M., et al., *Nonsteroidal anti-inflammatory drugs and peroxisome proliferator-activated receptor-gamma agonists modulate immunostimulated processing of amyloid precursor protein through regulation of beta-secretase.* J Neurosci, 2003. **23**(30): p. 9796-804.

50. Gad, E.S., S.A. Zaitone, and Y.M. Moustafa, *Pioglitazone and exenatide enhance cognition and downregulate hippocampal beta amyloid oligomer and microglia expression in insulin-resistant rats.* Canadian Journal of Physiology and Pharmacology, 2015. **94**(8): p. 819-828.
51. Quan, Q., et al., *Pioglitazone Reduces ß Amyloid Levels via Inhibition of PPARγ Phosphorylation in a Neuronal Model of Alzheimer's Disease.* Front Aging Neurosci, 2019. **11**: p. 178.
52. Camacho, I.E., et al., *Peroxisome-proliferator-activated receptor gamma induces a clearance mechanism for the amyloid-beta peptide.* J Neurosci, 2004. **24**(48): p. 10908-17.
53. Seok, H., et al., *Low-dose pioglitazone can ameliorate learning and memory impairment in a mouse model of dementia by increasing LRP1 expression in the hippocampus.* Scientific Reports, 2019. **9**(1): p. 4414.
54. Saunders, A.M., D.K. Burns, and W.K. Gottschalk, *Reassessment of Pioglitazone for Alzheimer's Disease.* Front Neurosci, 2021. **15**: p. 666958.
55. Geldmacher, D.S., et al., *A Randomized Pilot Clinical Trial of the Safety of Pioglitazone in Treatment of Patients With Alzheimer Disease.* Archives of Neurology, 2011. **68**(1): p. 45-50.
56. Gold, M., et al., *Rosiglitazone Monotherapy in Mild-to-Moderate Alzheimer's Disease: Results from a Randomized, Double-Blind, Placebo-Controlled Phase III Study.* Dementia and Geriatric Cognitive Disorders, 2010. **30**(2): p. 131-146.
57. Landreth, G., et al., *PPARγ agonists as therapeutics for the treatment of Alzheimer's disease.* Neurotherapeutics, 2008. **5**(3): p. 481-489.
58. Cheng, H., et al., *The peroxisome proliferators activated receptor-gamma agonists as therapeutics for the treatment of Alzheimer's disease and mild-to-moderate Alzheimer's disease: a meta-analysis.* International Journal of Neuroscience, 2016. **126**(4): p. 299-307.
59. *Therapeutic Potential of Peroxisome Proliferator-Activated Receptor Agonists for Neurological Disease.* 2003. **5**(1): p. 67-73.
60. Kirschenbaum, D., et al., *Quantitative 3D microscopy reveals a genetic network predicting the local activity of anti-Aß compounds.* 2021: p. 2021.01.15.426090.
61. Moosecker, S., et al., *Brain Expression, Physiological Regulation and Role in Motivation and Associative Learning of Peroxisome Proliferator-activated Receptor γ.* Neuroscience, 2021. **479**: p. 91-106.
62. Baranello, R.J., et al., *Amyloid-beta protein clearance and degradation (ABCD) pathways and their role in Alzheimer's disease.* Curr Alzheimer Res, 2015. **12**(1): p. 32-46.
63. Perlmutter, L.S., E. Barron, and H.C. Chui, *Morphologic association between microglia and senile plaque amyloid in Alzheimer's disease.* Neurosci Lett, 1990. **119**(1): p. 32-6.
64. Wisniewski, T., J. Ghiso, and B. Frangione, *Biology of A beta amyloid in Alzheimer's disease.* Neurobiol Dis, 1997. **4**(5): p. 313-28.
65. Combs, C.K., et al., *Identification of microglial signal transduction pathways mediating a neurotoxic response to amyloidogenic fragments of beta-amyloid and prion proteins.* J Neurosci, 1999. **19**(3): p. 928-39.
66. Koenigsknecht, J. and G. Landreth, *Microglial phagocytosis of fibrillar beta-amyloid through a beta1 integrin-dependent mechanism.* J Neurosci, 2004. **24**(44): p. 9838-46.
67. Bernardo, A. and L. Minghetti, *PPAR-gamma agonists as regulators of microglial activation and brain inflammation.* Curr Pharm Des, 2006. **12**(1): p. 93-109.
68. Pérez, M.J. and R.A. Quintanilla, *Therapeutic Actions of the Thiazolidinediones in Alzheimer's Disease.* PPAR Res, 2015. **2015**: p. 957248.
69. Fernandez-Martos, C.M., et al., *Combination treatment with leptin and pioglitazone in a mouse model of Alzheimer's disease.* Alzheimer's & Dementia: Translational Research & Clinical Interventions, 2017. **3**(1): p. 92-106.
70. Minatohara, K., M. Akiyoshi, and H. Okuno, *Role of Immediate-Early Genes in Synaptic Plasticity and Neuronal Ensembles Underlying the Memory Trace.* 2016. **8**.
71. Schreiber, S.S., et al., *Activation of immediate early genes after acute stress.* Neuroreport, 1991. **2**(1): p. 17-20.

72. Lu, W., et al., *Over-expression of c-fos mRNA in the hippocampal neurons in Alzheimer's disease.* Chin Med J (Engl), 1998. **111**(1): p. 35-7.
73. Rylski, M., et al., *JunB is a repressor of MMP-9 transcription in depolarized rat brain neurons.* Mol Cell Neurosci, 2009. **40**(1): p. 98-110.
74. Perez-Cruz, C., et al., *Reduced spine density in specific regions of CA1 pyramidal neurons in two transgenic mouse models of Alzheimer's disease.* J Neurosci, 2011. **31**(10): p. 3926-34.
75. Qin, X., Y. Wang, and H.K. Paudel, *Inhibition of Early Growth Response 1 in the Hippocampus Alleviates Neuropathology and Improves Cognition in an Alzheimer Model with Plaques and Tangles.* Am J Pathol, 2017. **187**(8): p. 1828-1847.
76. Minett, T., et al., *Microglial immunophenotype in dementia with Alzheimer's pathology.* Journal of Neuroinflammation, 2016. **13**(1): p. 135.
77. Waller, R., et al., *Iba-1-/CD68+ microglia are a prominent feature of age-associated deep subcortical white matter lesions.* PLoS One, 2019. **14**(1): p. e0210888.
78. Hüttenrauch, M., et al., *Glycoprotein NMB: a novel Alzheimer's disease associated marker expressed in a subset of activated microglia.* Acta Neuropathologica Communications, 2018. **6**(1): p. 108.
79. Scheckel, C., et al., *Ribosomal profiling during prion disease uncovers progressive translational derangement in glia but not in neurons.* Elife, 2020. **9**.
80. Sánchez-Navarro, A., et al., *An integrative view of serpins in health and disease: the contribution of SerpinA3.* 2021. **320**(1): p. C106-C118.
81. Zattoni, M., et al., *Serpin Signatures in Prion and Alzheimer's Diseases.* Molecular Neurobiology, 2022.
82. Habchi Johnny, Y.X., Jenkins kerry, Perni Michele, Sarwat Sunehera, Menzies Joseph, Campero Peredo Christina, Possenti Andrea, Linse Sara, Knowles Tuomas, Dobson Christopher, Cohen Samuel, Vendruscolo Michele, *THERAPY FOR PROTEIN MISFOLDING DISEASE*. 2019.
83. Bourin, M. and M. Hascoët, *The mouse light/dark box test.* Eur J Pharmacol, 2003. **463**(1-3): p. 55-65.
84. Takao, K. and T. Miyakawa, *Investigating gene-to-behavior pathways in psychiatric disorders: the use of a comprehensive behavioral test battery on genetically engineered mice.* Ann N Y Acad Sci, 2006. **1086**: p. 144-59.
85. Vuillermot, S., et al., *Schizophrenia-relevant behaviors in a genetic mouse model of constitutive Nurr1 deficiency.* 2011. **10**(5): p. 589-603.
86. Meyer, U., et al., *Towards an immuno-precipitated neurodevelopmental animal model of schizophrenia.* Neuroscience & Biobehavioral Reviews, 2005. **29**(6): p. 913-947.
87. Barker, G.R., et al., *Recognition memory for objects, place, and temporal order: a disconnection analysis of the role of the medial prefrontal cortex and perirhinal cortex.* J Neurosci, 2007. **27**(11): p. 2948-57.
88. Schalbetter, S.M., et al., *Adolescence is a sensitive period for prefrontal microglia to act on cognitive development.* Science Advances, 2022. **8**(9): p. eabi6672.
89. Rasmussen, J., et al., *Amyloid polymorphisms constitute distinct clouds of conformational variants in different etiological subtypes of Alzheimer's disease.* Proc Natl Acad Sci U S A, 2017. **114**(49): p. 13018-13023.
90. Yang, B., et al., *Single-cell phenotyping within transparent intact tissue through whole-body clearing.* Cell, 2014. **158**(4): p. 945-958.
91. Bria, A. and G. Iannello, *TeraStitcher - A tool for fast automatic 3D-stitching of teravoxel-sized microscopy images.* BMC Bioinformatics, 2012. **13**(1): p. 316.
92. Berg, S., et al., *ilastik: interactive machine learning for (bio)image analysis.* Nat Methods, 2019. **16**(12): p. 1226-1232.
93. Dadgar-Kiani, E., *Github.* 2020.

94. Smith, S.M. and T.E. Nichols, *Threshold-free cluster enhancement: Addressing problems of smoothing, threshold dependence and localisation in cluster inference.* NeuroImage, 2009. **44**(1): p. 83-98.
95. Sbalzarini, I.F. and P. Koumoutsakos, *Feature point tracking and trajectory analysis for video imaging in cell biology.* Journal of Structural Biology, 2005. **151**(2): p. 182-195.
96. Yayon, N., et al., *Intensify3D: Normalizing signal intensity in large heterogenic image stacks.* Scientific Reports, 2018. **8**(1): p. 4311.
97. Klein, S., et al., *elastix: A Toolbox for Intensity-Based Medical Image Registration.* IEEE Transactions on Medical Imaging, 2010. **29**(1): p. 196-205.

Figure 1

Figure 1

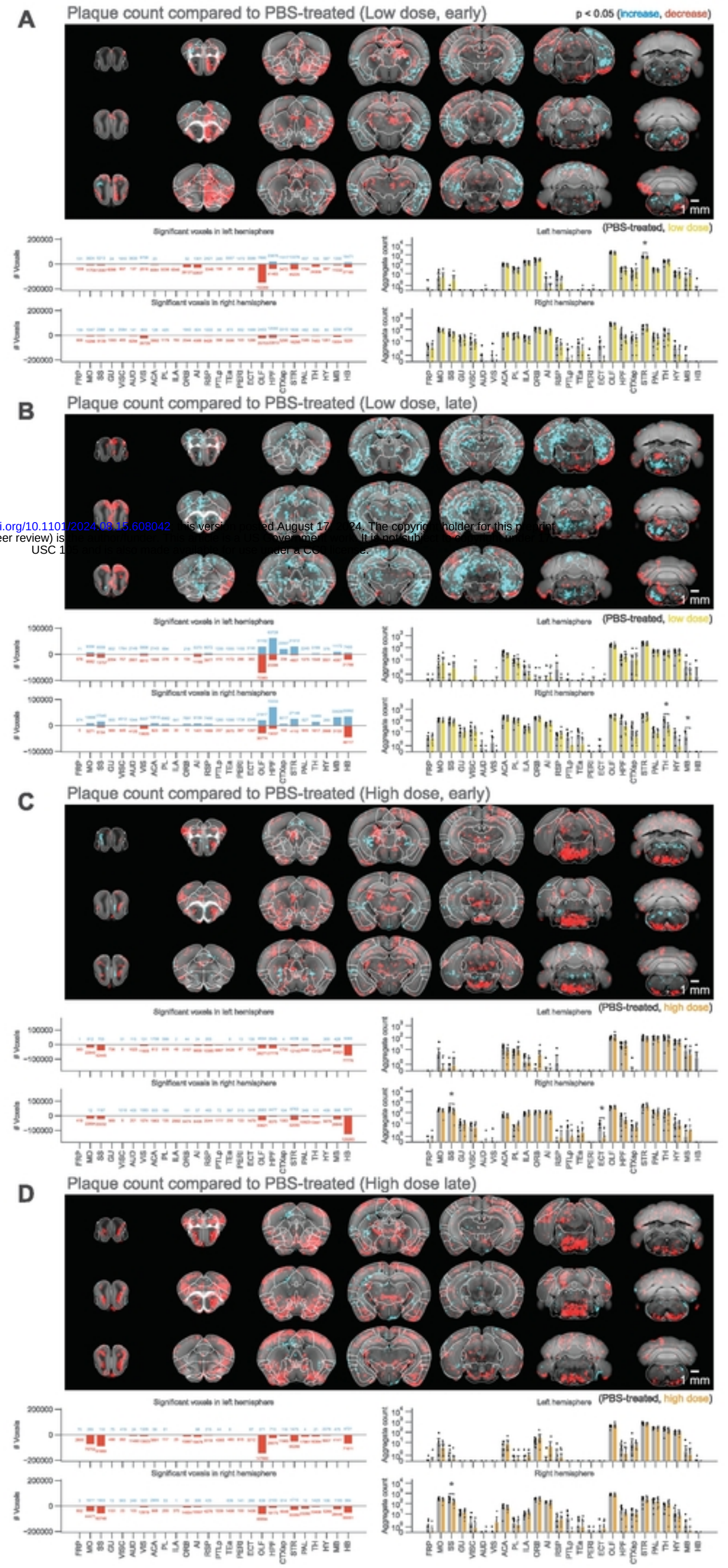

Figure 2

Figure 2

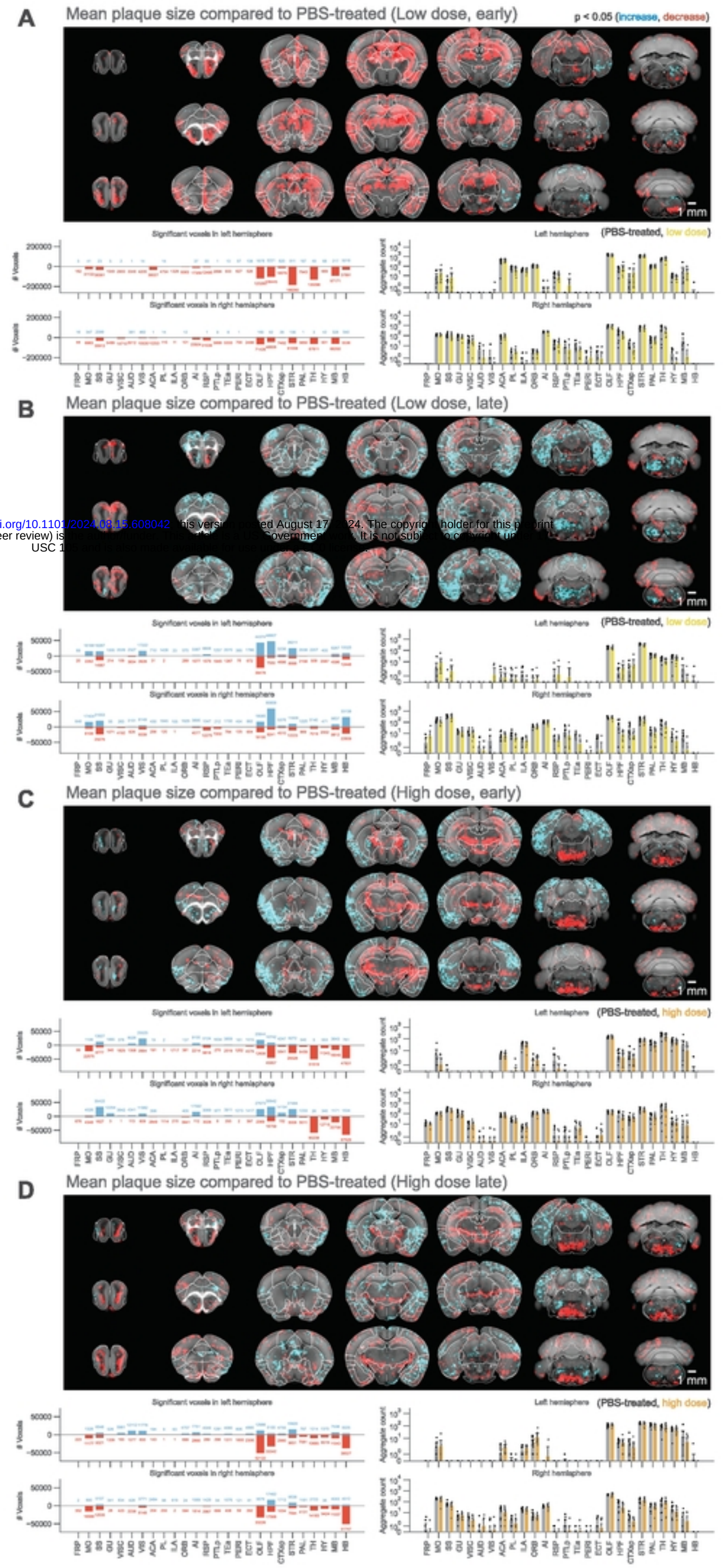

Figure 3

Figure 3

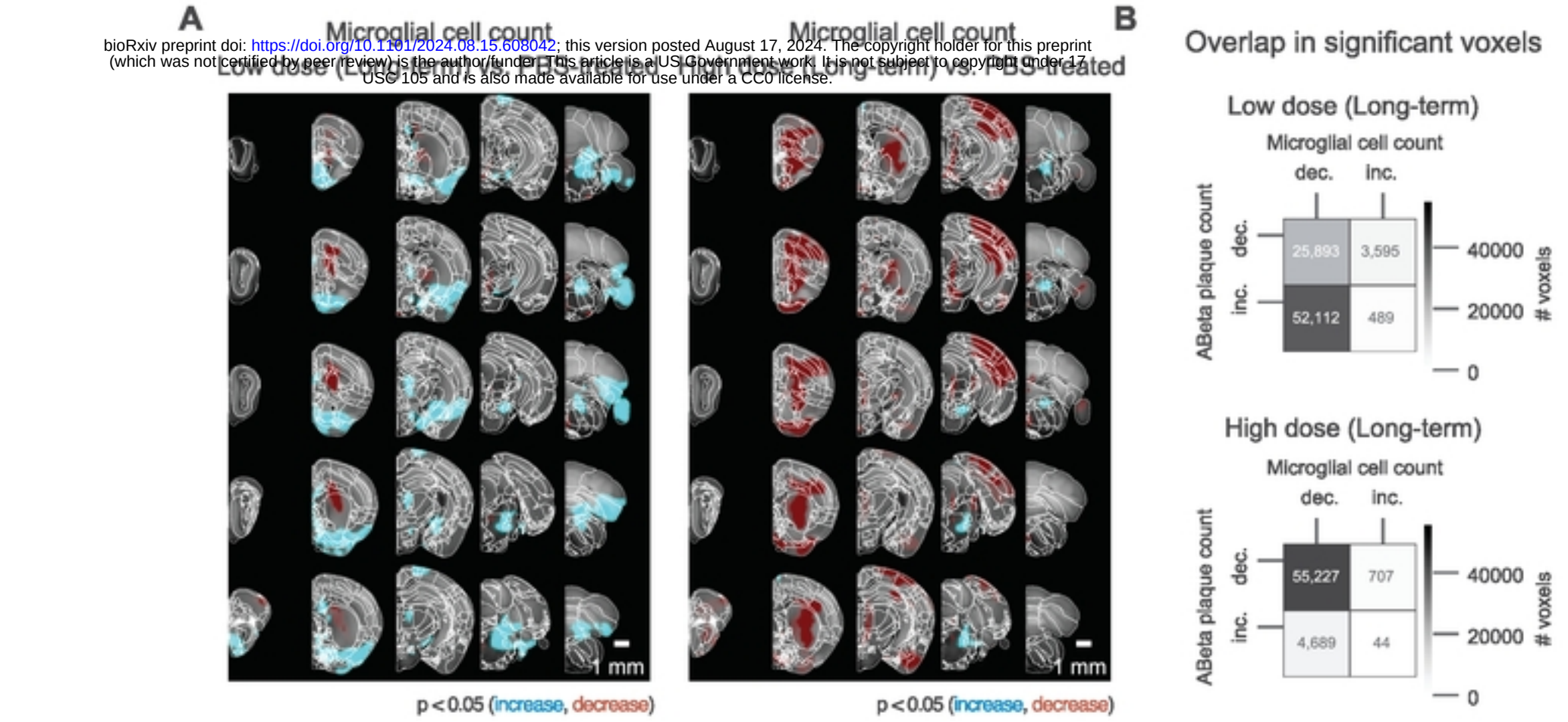

Figure 4

Figure 4

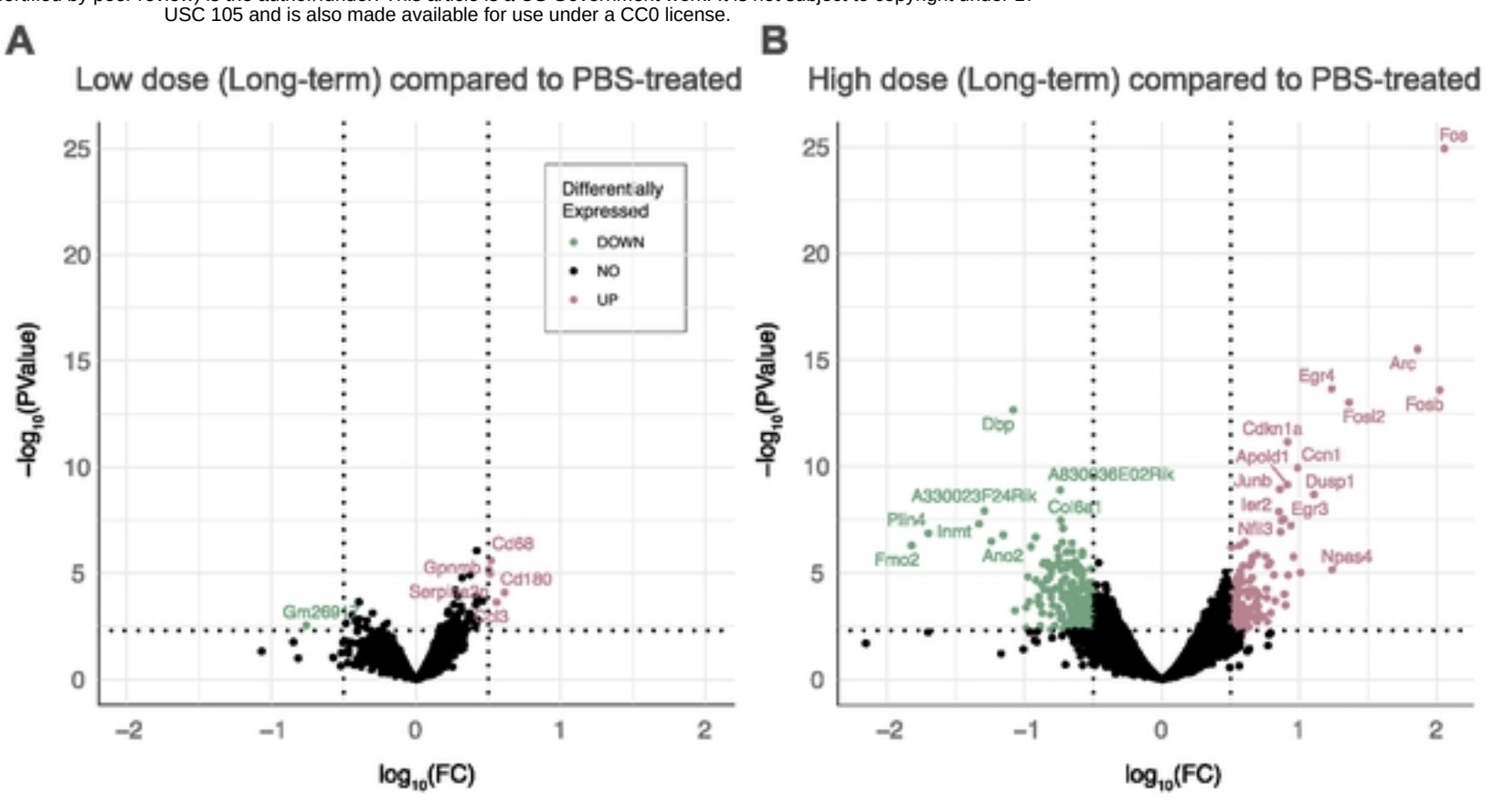

Figure 5

Figure 5